Optimizing Energy Conversion in Organic Materials via Processing and Morphological Design

by

Jojo A. Amonoo

A dissertation submitted in partial fulfillment
of the requirements for the degree of
Doctor of Philosophy
(Applied Physics)
in The University of Michigan
2016

Doctoral Committee:

Professor Peter F. Green, Chair
Professor Roy Clarke
Professor Jinsang Kim
Professor Richard E. Robertson
Associate Professor Anish Tuteja

Dedication

To my late father, Dr. Benjamin K. Amonoo, of blessed memory

Acknowledgement

As I prepare to draw the curtain on my doctoral studies, I would like to take this opportunity to express my sincerest gratitude to some special people who have been there for me, encouraging and supporting me, ultimately making my experience a memorable one I will cherish.

First and foremost, I would like to thank Professor Roy Clarke for his mentoring and kind support during my first year in the Applied Physics Ph.D. Program. As the Program Director then, Professor Clarke had an open-door policy and I was always welcome to walk in and discuss classes and research. It was at one of our meetings when I was still undecided about which research group to join that Professor Clarke recommended I set up a meeting with Professor Peter Green to discuss research opportunities; the rest is history. Professor Green welcomed me into his group and as my Ph.D. advisor has been supportive and patient in guiding me through my Ph.D. work and I am forever grateful. Also, my warmest appreciation goes to the rest of my dissertation committee, Professors Jinsang Kim, Richard Robertson and Anish Tuteja for their insights and time spent on assisting me in the completion of my work.

To all my past and present lab colleagues in the Green Group, what can I say? Thank you for making my day-to-day work life in the lab a fun-filled and challenging

experience and also for all the intellectually stimulating conversations, especially after group meeting. It has been an absolute pleasure working with all of you, Dr. Emmanouil Glynos, Dr. Carl McIntyre, Dr. Aaron Tan, Dr. Chelsea Chen, Dr. Jenny Kim, Dr. Bradley Frieberg, Dr. Hengxi Yang, Dr. Bingyuan Huang, Dr. Peter Chung, Junnan Zhao, Anton Li, Kyle Johnson, Ban Dong and Jill Wenderott. Research is a collaborative effort and thus I would like to extend a special thank you to my collaborators during my time here, Dr. David Bilby, Dr. Edmund Palermo, Dr. Kevin Bergemann, Dr. Steven Morris, Dr. Adam Barito, Dr. Matthew Sykes, Prof. Anne McNeil, Prof. Max Shtein and Prof. Stephen Forrest.

Finally, I would like to extend my heartfelt appreciation to my mother Grace Amonoo, who taught me that persevering and working diligently is often rewarded, and my brother Nana Kwame Amonoo, my sisters Ama Amevor and Maame Esi Wilson for their unconditional love and prayers as I embarked on this journey far away from the warm and sunny tropics of Ghana to the bitter cold winter in Michigan. Most importantly, I would not have been able to make it thus far without my loving wife Effie Amonoo, who has sacrificed a lot to support me while taking care of the kids. Effie, we certainly earned this doctoral degree together; this is as much yours as it is mine, my dear. Thank you for being my rock and number one cheerleader after all those strenuous long hours (mostly by the AFM) and ‘bad’ data days. Lastly, to my adorable son, Benjamin Amonoo and lovely daughter, Amy Amonoo, or Princess Amy as she likes to be called. Watching you guys grow and learn to walk and talk brings me so much joy and I thank you each day for saying “Yeah! Daddy is home” when I am back from the lab. All these have

certainly helped to put things in perspective and I am very grateful to God for my family and friends and all the assistance I have received for the completion of my thesis work.

Table of Contents

List of Figures

List of Tables

List of Publications

1. B. X. Dong, **J. Amonoo**, G.E. Purdum, Y.-L. Loo, P.F. Green, "The importance of polymer backbone orientation in determining carrier transport in poly(3-hexylthiophene) thin film transistors." *Manuscript in preparation*

2. M. E. Sykes, **J. Amonoo**, P. F. Green, M. Shtein, "Impact of heterojunction interface morphology on exciton management in small-molecular organic photovoltaics." *Manuscript in preparation*

3. **J. Amonoo**, A. Li, B. Huang, G. Purdum, M.E. Sykes, E. F. Palermo, A. J. McNeil, M. Shtein, Y.-L. Loo, P. F. Green, "An all-conjugated gradient copolymer approach for morphological control of Polymer Solar Cells." JOURNAL OF MATERIALS CHEMISTRY A*, 2015, 3, 20174*

4. A. Li, D. Bilby, B. X. Dong, **J. Amonoo**, J. Kim, P. F. Green, "Macroscopic alignment of poly(3-hexylthiophene) for enhanced long-range collection of photogenerated carriers." JOURNAL OF POLYMER SCIENCE, PART B: POLYMER PHYSICS DOI: 10.1002/polb.23888

5. O.L. Griffith, X. Liu, **J. Amonoo**, B. Song, X. Che, P. Djurovic, M. E. Thompson, P. F. Green, S. R. Forrest, "Charge transport and exciton dissociation in organic solar cells consisting of dipolar donors mixed with C_{70}." PHYSICAL REVIEW B 92, 085404

6. K.J. Bergemann, **J. Amonoo**, B. Song, P.F. Green, S.R. Forrest, "Surprisingly high conductivity and efficient exciton blocking in fullerene:wide-energy-gap small molecule mixtures." NANO LETTERS 2015, 15 (6), 3994–3999

7. A. Li, **J. Amonoo**, B. Huang, P. K. Goldberg, A. J. McNeil, P.F. Green, "Enhancing photovoltaic performance using an all-conjugated random copolymer to tailor bulk and interfacial morphology." ADVANCED FUNCTIONAL MATERIALS, 2014, 24, 5594–5602

8. B. Huang, **J. Amonoo**, A. Li, X. C. Chen, P. F. Green, "Role of domain size and phase purity on charge carrier density, mobility and recombination in P3HT:$PC_{61}BM$ devices." JOURNAL OF PHYSICAL CHEMISTRY C, 2014, 118 (8), 3968

9. M. E. Sykes, A. Barito, **J. Amonoo**, P. F. Green, M. Shtein, "Broadband plasmonic photocurrent enhancement in planar organic photovoltaics embedded in a metallic nanocavity." ADVANCED ENERGY MATERIALS, 2014, 1301937

10. A. Barito, M. E. Sykes, D. Bilby, **J. Amonoo**, Y. Jin, S.E. Morris, P. F. Green, J. Kim, M. Shtein, "Recovering lost excitons in organic photovoltaics using a transparent dissociation layer." JOURNAL OF APPLIED PHYSICS, 2013, 113 (20), 203110

11. D. Bilby, **J. Amonoo**, M. E. Sykes, B. Frieberg, B. Huang, J. Hungerford, M. Shtein, P. F. Green, J. Kim, "Reduction of open circuit voltage loss in polymer photovoltaic cell via interfacial molecular design: Insertion of a molecular spacer." APPLIED PHYSICS LETTERS, 2013, 103, 203902

12. **J. Amonoo**, E. Glynos, X.C. Chen, P.F. Green “An alternative processing strategy for organic photovoltaic devices using a supercritical fluid” JOURNAL OF PHYSICAL CHEMISTRY C, 2012, 116 (39), 20708

Abstract

The performance and reliability of bulk heterojunction thin film polymer solar cells are intricately linked to the three-dimensional nanoscale morphological structure of the photoactive materials, driven by the extent of phase separation between the polymer and fullerene components. To this end, well-established processing protocols to induce phase separation comprising high temperature and solvent vapor annealing have been employed to create optimal nanoscale morphologies. This thesis examines two fundamental approaches regarding the control of nanoscale morphology: (1) a novel environmentally benign processing method, and (2) the use of an all-conjugated gradient copolymer.

Recently, liquid and supercritical carbon dioxide ($scCO_2$) have emerged as viable alternatives to toxic organic solvents in polymer processing. We introduce a new and environmentally friendly alternative strategy utilizing $scCO_2$ for processing and morphology control of the archetypal bulk heterojunction organic photovoltaic system poly(3-hexylthiophene) (P3HT)/phenyl-C_{61}-butyric acid methyl ester ($PC_{61}BM$) system. The density-dependent solvating strength of $scCO_2$ can be regulated with fine changes to its pressure and/or temperature. We found that under appropriate conditions of pressure and temperature, devices exhibited efficiencies that were comparable to, or exceeded,

those achieved using conventional techniques, albeit with similar nanoscale morphologies. The enhanced efficiency achieved using $scCO_2$ is associated with a larger fraction of photoactive regions as revealed from photoconductive-atomic force microscopy measurements and much purer polymer- and fullerene-rich phases as seen with energy-filtered transmission electron microscopy (EFTEM) and electron energy loss spectroscopy.

For the second route, using an all-conjugated copolymer approach through molecular design of 3-hexylselenophene and 3-hexylthiophene in block and gradient sequence architectures, we show that for the same overall copolymer composition, the ordering of molecular constituents along the copolymer chain (copolymer sequence) significantly influenced the nanoscale morphology and phase separation behavior. Relative to the block copolymer:PCBM, the gradient copolymer:PCBM sample formed a more uniform, continuous and interconnected network of polymer fibrils within the acceptor-rich phase, associated with a large D/A interface as revealed by EFTEM. Furthermore, charge extraction of photogenerated carriers by linearly increasing voltage showed that the gradient copolymer:PCBM device possessed the highest initial carrier density, consistent with a larger D/A interfacial area, though at the expense of increased carrier recombination rate.

CHAPTER 1:

Introduction

This chapter introduces the motivation for this work and basic working principles of the polymer-based photovoltaic devices investigated. We also make the case for the importance of morphology control of bulk heterojunction organic solar cells.

1.1 Motivation and Background

Developing innovative technologies that harness clean and renewable energy resources is critical for environmental sustainability. With global demand for energy expected to almost double by 2050[1] due to population and economic growth, continuation of the "business as usual" approach with modern society's considerable reliance on traditional fossil fuel-based technologies raises concerns of global warming and climate change. Additionally, the global energy landscape is evolving at a fast pace and in assessing options for mitigating climate change, there is no one-size-fits-all solution as natural resource endowments vary across geographical locations and approaches should be feasible and practical for different socio-economic settings.[2] Mitigating technologies being explored in scenarios to reduce carbon emissions have included, advanced energy efficiency measures, improved forest management and crop cultivation and switching to low-carbon energy sources (biomass, carbon sequestration, hydroelectric, tidal, nuclear,

geothermal, wind and solar) with a higher share of renewables.[2] The U.S. Energy Information Administration (EIA) reports that about 21% of world electricity generation was from renewable energy in 2011[3], with a projection for nearly 25% in 2040.[4] In order to meet this growing demand, renewable energy technologies must be able to scale-up and also remain competitive relative to their fossil fuel counterparts.

The earth receives in an hour enough energy from the sun to meet global demand for a year, about 1.0×10^9 TWh/year. This suggests that emerging technologies that are developed based on the photo-conversion of sunlight directly into electricity, at low-cost, are an attractive long-term strategy that promises a sustainable energy future; ergo, organic photovoltaics (OPVs). With the current PV market dominated by inorganic PV technologies (Si, GaAs, CdTe, CdS, etc.),[5] which require the mining of rare earth elements and energy intensive fabrication processes at higher costs, OPVs look more promising for cost-effective energy production. This is due to the fact that organic materials can be processed at lower temperatures or from solution, making them compatible with low-cost substrates such as flexible plastics or metal foils, and can also be deposited via high-throughput roll-to-roll production processes. Furthermore, through chemical synthetic routes and molecular design, organic materials provide a limitless availability of environmentally safe materials. However, with low device efficiency and operating lifetimes plaguing OPV technologies, considerable improvements in efficiency and shelf life are certainly required before commercialization. To this end, much fundamental research into device physics and operation mechanisms is required to allow for the burgeoning field of OPVs to be truly economically viable and competitive for

large-scale energy production. The intention of the work presented here is to contribute to fundamental research in the OPV field in order to further understand the structure-property-performance relationship in OPV devices, in this way, assisting in the design of the next generation of high performance and reliable polymeric materials.

1.2 Dissertation Outline

This dissertation is organized as follows: the remainder of chapter 1 is devoted to introducing organic semiconductor materials, specifically π-conjugated polymers along with the physics of optoelectronic processes accompanying OPV device operation. Chapter 2 introduces a novel processing procedure for polymer-based PV devices using supercritical carbon dioxide. This was the first time an environmentally friendly solvent was utilized for OPV device processing; typically volatile organic solvents are used. In Chapter 3 we report on our results of utilizing an all-conjugated gradient copolymer as the primary donor material for morphology control and device stability in polymer solar cells. In Chapter 4 we present a proof of concept in developing and extending the capabilities of kelvin probe force microscopy, a scanning probe microscopy technique used for conducting and semiconducting materials, to study phase separation in insulating polymers. We finally end with conclusions and outlook for this work in Chapter 5.

1.3 Organic Semiconductors

Organic semiconductors are a class of carbon-rich compounds that have garnered intense interest worldwide as promising for low-cost manufacturing, lightweight and flexible form factors for innovative developments in lighting, photovoltaic and electronic devices. There are two primary categories of organic semiconductors: small molecular

semiconductors and π-conjugated polymers. This work focuses on conjugated polymer-based devices. The semiconducting properties of conjugated polymers emanate from the sp^2-hybridization of carbon atoms, leading to an alternating single and double bond structure. Neighboring p_Z-orbitals of each sp^2-hybridized carbon atom overlap and form π-bonds resulting in the delocalization of π-electrons over the polymer backbone, and the formation of a band-like structure. Since the electrons are delocalized, they can move freely between atoms and do not belong to a single atom, but rather to a group of atoms.[6] The highest occupied molecular orbital (HOMO), and lowest unoccupied molecular orbital (LUMO) are hence analogous to the valence and conduction bands in inorganic semiconductors. The distance along the backbone, over which the p_Z-orbitals overlap between polymer chains and electrons are delocalized, is known as the conjugation length. These π-bonds are thus the source of charge transport in conjugated polymers giving rise to their characteristic semiconducting properties.[7]

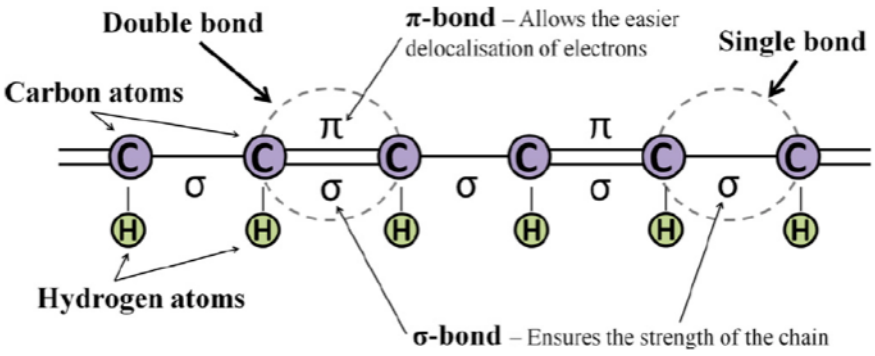

Figure 1.1 A simplified schematic of a π-conjugated polymer backbone: a chain containing alternating single and double bond, from Ref [8].

An important distinction to inorganic semiconductors is the fact that organic semiconductors have lower charge-carrier mobilities due to weaker electronic coupling and a thermally-activated hopping mechanism for transport,[9] however, they possess much

higher absorption coefficients ($\geq 10^5$ cm^{-1}) resulting in high absorption in thin films on the order of 100 nm. Furthermore, organic semiconductors possess very low dielectric constants (typically between 2 - 4). So that photo-excitation in organic semiconductor materials at room temperature generally results in the formation of bound electron-hole pairs known as excitons, rather than free charge carriers as in inorganic semiconductors.

Excitons, when generated, can typically diffuse randomly through organic materials on a length scale of 5 - 20 nm before they either decay to the ground state or recombine;[10] this is known as the exciton diffusion length (L_D). When an exciton is formed, the hole would reside in the HOMO while the electron is in the LUMO of one molecule. In order for free carriers to be generated the excitons have to be dissociated and separated within their lifetime.

1.4 Polymer OPV Working Principle

Effective charge photogeneration in organic solar cells therefore requires the dissociation of excitons at a heterojunction or donor/acceptor interface,[11] consisting of two dissimilar organic materials with HOMO and LUMO levels offset in a staggered fashion, as in Figure 1.2, creating an energy offset necessary to trigger exciton dissociation. Typically, the conjugated polymer serves as the donor (D) material while the fullerene derivative as the acceptor (A).

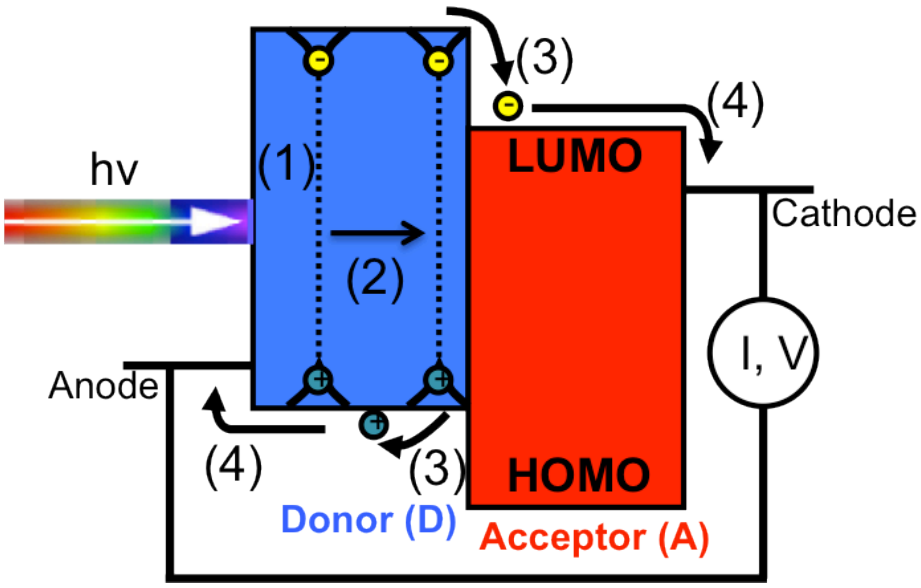

Figure 1.2 Energy diagram of an organic heterojunction showing the charge photogeneration process, from exciton generation (1) to charge collection (4) at the electrodes. Electrons (-) are colored yellow and holes (+) are green.

In a typical polymer solar cell device the photoactive layer, responsible for light absorption and charge generation, consists of a blend of a donor polymer, which transports holes, and fullerene acceptor, which transports electrons. The cathode collects electrons and the anode collects holes. There are also buffer layers between the photoactive layer and each electrode responsible for work function modification and efficient charge collection. The step-by-step process of photocurrent generation illustrated in Figure 1.2 is as follows: (1). An absorbed photon creates an exciton (2). Exciton diffuses randomly with a probability of finding a D/A interface (3). Exciton dissociation and charge transfer may occur creating free carriers (4). Carrier transport to respective electrodes. The performance of photovoltaic devices is characterized by the current density-voltage behavior, shown in Figure 1.3. The performance indicators are the short circuit current density (J_{SC}) which is current density at no applied bias, the open

circuit voltage (V_{OC}) which is the external bias applied to completely reduce the current to zero, the fill factor (*FF*) which defines the quality of the photovoltaic device relates to the J_{SC}, V_{OC}, and overall power conversion efficiency (PCE) where PCE = (J_{SC} V_{OC} *FF*)/P_{in}, and P_{in} is the incident power density.

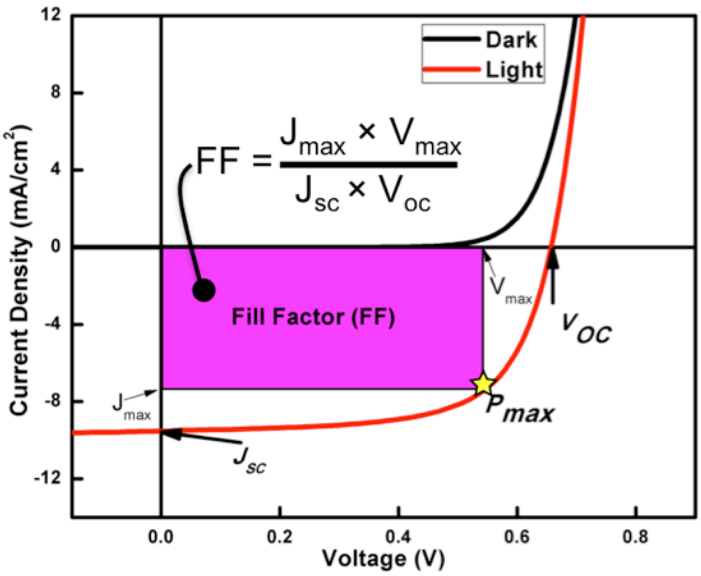

Figure 1.3 A representative current density-voltage (J-V) curve of a polymer solar cell device under dark (black) and light (red) conditions. Performance indicators as described in the text are shown in the diagram.

As discussed earlier, organic materials have relatively short L_D (5 - 20 nm) but can absorb in thickness range of 100 nm. This mismatch in length-scales limits the thicknesses and dimension requirements of OPVs. However, this bottleneck has been overcame by the utilization of bulk heterojunction (BHJ) thin films consisting of a interpenetrating network of D and A materials[12,13] processed from a blend solution and cast via spin coating or other thin film deposition techniques. In this instance, The D/A interfacial area (A_{intf}) is maximized and distributed throughout the bulk volume of the composite film enabling efficient exciton dissociation and charge generation. During

device operation an exciton upon reaching the D/A interface, transfers the electron to the acceptor while the hole resides in the donor material, charges are then transported to their respective electrodes via a percolated phase-separated network on the order of L_D, in the presence of the internal electric field resulting from the difference in work function of the anode and cathode. Consequently, controlling the purity, length-scales of the D and A phases, together with the spatial organizational structure and hence the morphology of polymer BHJ solar cells is critical for efficient charge generation and transport and ultimately enhanced device performance.

1.5 Active Layer Morphology Control

Recently, there have been many advances in the optimization of the morphology of BHJ polymer-fullerene solar cells by utilizing thermal annealing, solvent-vapor annealing and solvent additive protocols in order to achieve phase-separated structures and improve device performance.[14-16] Typically, solvent cast samples from polymer-fullerene blends are composed of crystalline regions of the polymer, fullerene aggregates and large amorphous polymer regions with molecularly dissolved fullerene.[17] Thermal treatment by placing the thin film deposited onto a transparent conducting substrate, such as indium tin oxide (ITO), onto a hot plate at a designated temperature changes the macro- and nanoscale morphology. Because the fullerene and polymer are usually miscible, the macroscopic morphology is determined by a competition between the diffusion of fullerene and the rate of crystallization of the polymer.[17,18] During thermal annealing, the fraction of the polymer amorphous regions decreases; additionally the extent of phase separation between the polymer and fullerene components increases and the polymer phase increases in purity and crystallinity.[17,18] The device PCEs are known to

improve after heating for a specific interval at a specified temperature, typically 150 ^{o}C. Beyond this time interval, the fullerene phase is known to increase appreciably in size, thereby reducing A_{intf}, leading to decreased PCEs. Clearly, the optimal morphology is not a true thermodynamic equilibrium morphology. The ideal morphology for efficient device performance is therefore one associated with optimal phase separation, that would maximize A_{intf}, while maintaining D and A domains, with optimal sizes on the order of L_D, high phase purity and crystallinity, that provide pathways to the electrodes.[19,20] This is the driving force for work presented in this dissertation.

1.6 Experimental Techniques

Various thin film characterization methods were used to probe both structural and electrical properties of the systems investigated. Device fabrication, testing, carrier dynamics, UV-visible absorption and atomic force microscopy measurements were done in-house in our laboratory. External quantum efficiency measurements were performed in Prof. Max Shtein's laboratory, energy filtered transmission electron microscopy was done in EMAL while Grazing incidence X-ray diffraction (GIXRD) was performed at Cornell University by our collaborators at Princeton University.

CHAPTER 2:

An Alternative Processing Strategy for Organic Photovoltaic Devices Using a Supercritical Fluid

2.1 Introduction

The design and fabrication of efficient solar cells depends on maximizing the absorption of solar energy and minimizing parasitic losses throughout the conversion process that leads to free carriers harvested at the electrodes.[21,22] In polymeric solar cells based on the donor/acceptor (D/A) blend, bulk-heterojunction (BHJ) concept, the spatial organizational structure, length-scales and purity of the D-rich and A-rich phases, and the D/A interfacial regions, play a significant role toward dictating the power conversion efficiency (PCE) of the cells.[21-23] The interfacial area between the D/A phases, A_{intf}, should be maximized, while the domain sizes should be optimized.[24-27] Excitons, formed due to the absorption of light should be in proximity of a D/A interface, to which they may migrate, with minimal recombination, for subsequent separation into free carriers.[28]

The dimensions and structure (purity/crystallinity) of the D and A-phases, influence transport and bimolecular recombination of free carriers. Bimolecular recombination is known to be significant in highly phase mixed systems and therefore reduces the J_{SC}.[28] The power conversion efficiency (PCE): PCE (%) = J_{SC} V_{OC} FF/P_{in}, where P_{in} is the incident power density, and FF is the fill factor of the device. The open circuit, V_{OC}, is to first order, determined by the HOMO level of the donor to the LUMO level of the acceptor; it is mediated by energetic disorder in the system.[29,30] The PCE is clearly influenced by the macro-scale and nanoscale morphology of the D/A blend.

OPV devices using poly(3-hexylthiophene) (P3HT) as the donor and phenyl-C_{61}-butyric acid methyl ester ($PC_{61}BM$) as the acceptor, have by far received the most attention than any other polymer based system.[31] In this regard, the P3HT/$PC_{61}BM$ system is considered a benchmark. Efficient device performance is associated with optimal phase separation, that would maximize A_{intf}, while maintaining domains, with optimal sizes, purity and crystallinity, providing pathways to the electrodes.[19,20] The best improvements in efficiencies have been achieved by using solvent additives prior to casting and subsequent thermal annealing.[16,32-35] Notably, Moule and Meerholz demonstrated that devices with active materials prepared using a mixed, nitrobenzene/chlorobenzene, solvent, exhibited the best performances.[33]

Herein we show that OPV devices made using P3HT/$PC_{61}BM$ and processed using supercritical carbon dioxide ($scCO_2$) exhibit comparable, and in some cases better, PCEs than devices prepared using the conventional thermal annealing protocols. $ScCO_2$ is a non-toxic compressible solvent with a critical point close to room temperature (T_C = 31.1 ºC and P_C = 7.38 MPa). The quality of the solvent is readily varied by changing

pressure, P, and temperature, T, in the range 35 - 70 ºC. Energy-filtered transmission electron microscopy (EFTEM) studies reveal that the $scCO_2$ processed devices possess similar macro- and nanoscale morphologies to those processed using the high temperature annealing protocol. The $scCO_2$ devices that exhibit better J_{SC}s and PCEs possessed P3HT and $PC_{61}BM$ phases that are comparable to those produced using the high temperature thermal annealing protocol and purer than the as-cast device, with a higher local degree of order/packing. We also learned from the photoconductive AFM measurements that only a fraction of the entire cross sectional area of a device was photoactive; the devices that exhibited the highest J_{SC}s and PCEs possessed largest photoactive areas.

2.2 Experimental Section

Materials. We examined conventional BHJ devices made from 1:1 by weight blends of P3HT (~ 95% RR, Rieke Metals, Inc., Lincoln, NE) and $PC_{61}BM$ (99.5% pure, American Dye Source Inc, Quebec, Canada). Pre-patterned ITO-coated glass substrates (Delta Technologies Ltd., Stillwater, MN) were cleaned by ultrasonication in acetone and isopropyl alcohol at 40 ºC for 20 min each, immediately followed by UV ozone treatment (Jelight Company Inc, model 342) for another 10 min. A poly(3,4-ethylenedioxythiophene) poly(styrenesulfonate) (PEDOT:PSS) (H.C. Starck Clevios PH500) layer was spin-coated onto the cleaned substrate and then baked at 120 ºC for 20 min under nitrogen purge on a hot plate, yielding a 60 nm thick PEDOT:PSS layer.

Experimental Procedure. The active layer was then prepared as follows. 10 mg P3HT and 10 mg $PC_{61}BM$ were dissolved in 1 ml of chlorobenzene and stirred for ~ 24 hrs in a nitrogen glove box. The blend solution was then filtered using 0.45 μm Teflon

Millipore filter before adding 7 vol% of nitrobenzene and the final solution stirred for ~ 5 min before spin-coating. This particular concentration was chosen to ensure 100% formation of aggregated nanodomains of pure P3HT.[33] The active layer was spin-coated from the final solution at 1000 rpm for 30 seconds and additionally spun at 3000 rpm for 2 min to further dry the solvent completely to give a final active layer thickness of 120 ± 15 nm.

The samples were then annealed for 5 minutes at 150 ºC, which was found to be the time to produce optimal morphologies with the highest PCEs and J_{SC}. A separate series of samples were also produced following the same procedure and processed in $scCO_2$, instead of high temperatures in order to a achieve phase separated morphologies. The samples were loaded into a stainless steel cell, which had been purged twice using CO_2 (Cryogenic gases, purity 99.98%) before commencing the annealing procedure. The cell, containing the samples, was then immersed in a water bath and heated to the desired temperature, which was controlled by a PID temperature controller. CO_2 was then charged to the cell using a manual pressure generator (High-Pressure Equipment Co.), with the pressure being monitored with a strain gauge pressure transducer (Sensotec). Post annealing, the cell was immersed in an ice bath during slow depressurization of ~ 1.59 MPa/min. We note from experiments in our laboratory that $scCO_2$ solvent swells and plasticizes P3HT; the effect can be varied based on T and P. Such effects on $PC_{61}MB$, are minimal and hardly evident.

Device fabrication was then finalized by depositing the top electrode consisting of a 100 nm Al layer on 1 nm thick LiF through a shadow mask under 4 x 10^{-7} Torr in an Angstrom Engineering PVD system. Devices were then characterized under ambient

conditions, using an Oriel solar simulator with illumination intensity of 100 mW/cm^2, AM 1.5G, together with a Hewlett Packard Semiconductor Parameter Analyzer.

The morphology of the fabricated devices was examined using energy-filtered transmission electron microscopy (EFTEM) in a JEOL 2100F TEM, equipped with a Gatan #863 Tridiem imaging filter (GIF), operated at an acceleration voltage of 200 kV. The active layer of the devices were floated from deionized water and picked up onto copper grids (Ted Pella, Inc.) prior to TEM. Electron energy loss spectroscopy (EELS) was also performed on neat P3HT and $PC_{61}BM$ thin films. EFTEM spectral images were collected using an energy slit width of 8 eV and a step width of 0.8 eV, from -5 eV to 40 eV, covering the zero loss regime and plasmon loss regime on the energy loss spectra.

Conductive- and photoconductive-AFM measurements were performed under ambient conditions using Asylum Research MFP-3D. A Pt/Ir5 coated contact-mode AFM probe (NanoWorld, CONTPt, spring constant 0.2 N/m) was used as the top contact for all measurements, tracking topography and current measurement simultaneously. A 532 nm diffraction limited laser was used to illuminate the sample for photocurrent measurements. The illumination intensity was on the order of 10^4 W/m^2 for all samples. Finally, ultraviolet-visible (uv-vis) absorption spectroscopy and XRD measurements were performed using a Varian 50Bio UV-Visible Spectrophotometer and a Rigaku MiniFlex X-Ray Diffractometer to gain additional insight into the structure of these samples.

2.3 Results and Discussion

The current–voltage characteristics of the P3HT/$PC_{61}BM$ devices processed under different conditions are plotted in Figure 2.1. While the V_{OC} values of all devices are

comparable, the as-cast device exhibited the lowest J_{SC} and the lowest PCEs, as expected. We note that in laboratories around the world, devices with active materials composed of nominally the same components exhibit PCEs that vary appreciably, for many reasons: device architecture, electrodes and buffer layer materials, and batch to batch variations in polymer synthesized from the same source or different sources, polymer molecular weight, chain tacticity etc.[31] However, for a given P3HT/PC_{61}BM system, involving identical materials, from the same batch, and identical device fabrication procedures, the best efficiencies are achieved by a solution-processing step, followed by annealing at elevated temperatures, for a specific time interval.

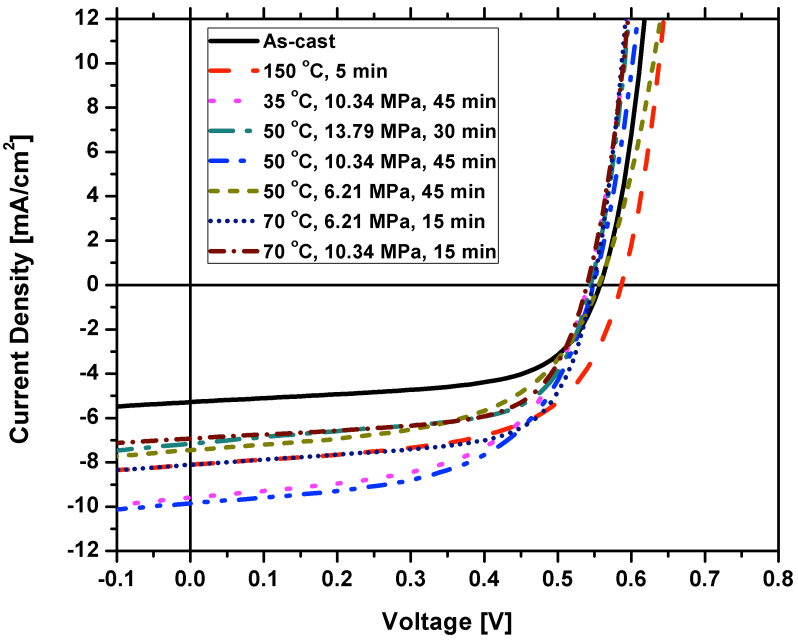

Figure 2.1 Current density-voltage curves of P3HT/PC_{61}BM blend prepared from chlorobenzene with 7 vol% nitrobenzene, for as-cast, thermal annealed at 150 ºC, 5 min, and $scCO_2$-processed at different temperatures and pressures for varying times

A summary of device characteristics is provided in Table 2-1. These values were not corrected for spectral mismatch. Devices annealed at T = 50 ºC and a pressure of P =

10.34 MPa, for 45 minutes, exhibited the best results. While the series resistance, R_s, and V_{OC} of all devices were comparable, regardless of the processing method, the J_{SC} is highest for the devices processed using this particular $scCO_2$ protocol. The performances of the optimized $scCO_2$ processed devices for a particular temperature, pressure and annealing time were consistently better than the as-cast devices, thereby demonstrating the effectiveness of scCO2 annealing toward enhancing device performance.

	PCE (%)	J_{SC} **(mA/cm^2)**	V_{OC} **(V)**	**FF (%)**	R_{sh} **(Ωcm^2)**	R_s **(Ωcm^2)**
As-cast	1.7 ± 0.1	5.2 ± 0.1	0.56 ± 0	60.0 ± 1.5	474	2.2
150 ºC, 5 min	2.6 ± 0.3	8.0 ± 0.2	0.59 ± 0	59.0 ± 2.0	418	2.4
50 ºC, 10.34 MPa, 45 min	2.9 ± 0.2	9.3 ± 0.6	0.54 ± 0.01	56.0 ± 2.0	356	2.7

Table 2-1 Device performance indicators of P3HT/PC61BM blend prepared from chlorobenzene with 7 vol% nitrobenzene, for as-cast, thermal annealed at 150 ^{o}C, 5 min, and scCO2 processed at 50 ^{o}C, pressure of 10.34 MPa for 45 min.

Device performance indicators of P3HT/PC_{61}BM blend prepared from chlorobenzene with 7 vol% nitrobenzene, for as-cast, thermal annealed at 150 ºC, 5 min, and $scCO_2$ processed at 50 ºC, pressure of 10.34 MPa, for 45 minutes.

Further details regarding the role of $scCO_2$ processing on device performance are provided in Figure 2.2, where it is shown that changes in temperature and pressure are associated with changes in device performance. The data in Figure 2.2(a) illustrate the effect of pressure and annealing time on the PCE of the devices at T=50 ºC, while those data in Figure 2.2(b) illustrate the effect of temperature at P=10.34 MPa and different annealing times. It is clear that an optimal processing time is required to achieve the best characteristics; device performances diminish after sufficiently long processing times.

Experiments were performed at other temperatures and $scCO_2$ pressures for different times; the information in Figure 2.3 shows the density-pressure phase diagram

for CO_2. The red symbols identify the pressures and temperatures at which devices where annealed for varying times with the corresponding density (solvating power) of $scCO_2$ and near-critical CO_2 at these conditions. While these other conditions did not yield optimal performances, their performances were better than the as-cast samples.

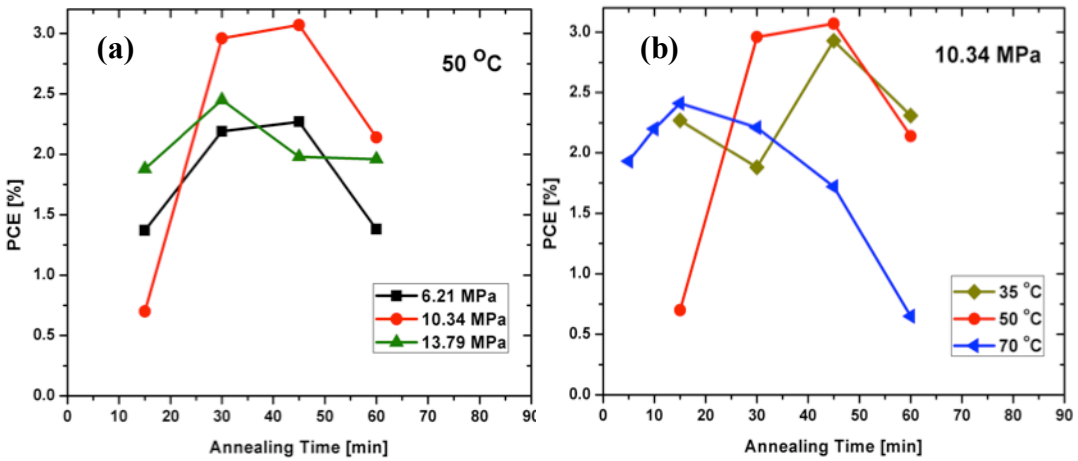

Figure 2.2 (a) Effect of pressure and (b) Effect of temperature and annealing time on PCE

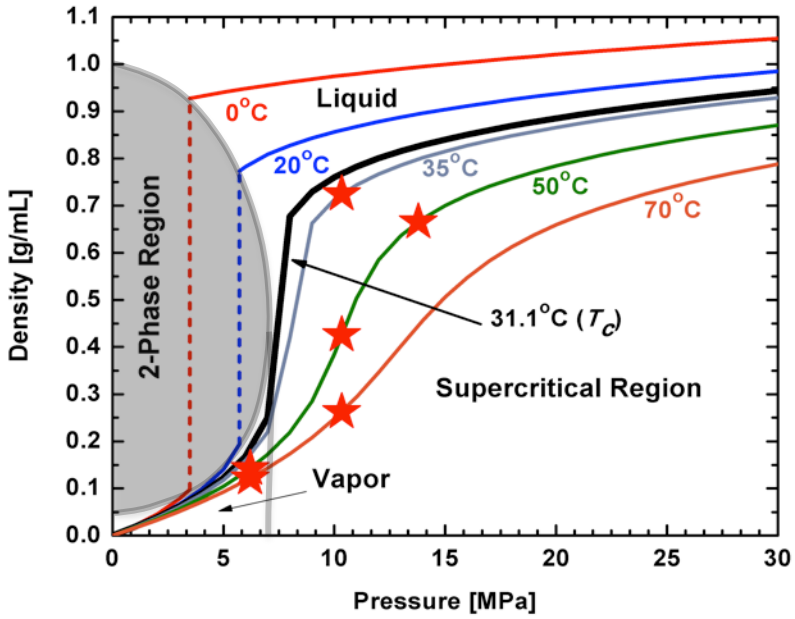

Figure 2.3 The density-pressure phase diagram for CO_2, the red stars indicate pressure/temperature annealing conditions investigated. Data provided by E. W. Lemmon, M. O. McLinden, D. G. Friend, Thermophysical Properties of Fluid Systems in NIST Chemistry WebBook, NIST Standard Reference Database Number 69 (Eds: P. J. Linstrom, W. G. Mallard)

We now discuss the morphological structure of the samples in order to understand the role of the supercritical solvent. Numerous studies have been devoted to understanding the morphological features of the P3HT/$PC_{61}BM$ system, the role of annealing temperature on the structure and the correlation between device performance and morphology.[36-39] Solvent cast samples are composed of crystalline regions of P3HT, $PC_{61}BM$ aggregates and large amorphous regions in which $PC_{61}BM$ molecules are dissolved within the amorphous P3HT regions.[17] The requirement for domains to be of a critical size is important; when the $PC_{61}BM$ phase is too small, particularly if its molecularly dissolved in P3HT, the number of charge transfer (CT) complex (polaron pairs) is high, but the bimolecular recombination rate is very high, leading to a lower J_{SC}.[40,41]

Heating the structure above 100°C changes the macro- and nano-scale morphology. Because $PC_{61}BM$ and P3HT are miscible the macroscopic morphology is determined by a competition between the diffusion of $PC_{61}BM$ and the rate of crystallization of P3HT. [17,18] During thermal annealing of a sample cast from a freshly made solution, the fraction of the P3HT amorphous regions decreases; additionally the extent of phase separation between the P3HT and $PC_{61}BM$ components increases and the P3HT phases increase in purity and crystallinity.[17,18] The P3HT domain sizes increase primarily along the a-direction (alkyl-stacking). The device PCEs are known to be maximized after heating for a specific interval at a specified temperature. Beyond this time interval, the $PC_{61}BM$ phase is known to increase appreciably in size, thereby reducing A_{intf}, leading to decreased PCEs. Notably the same trends are exhibited by the

$scCO_2$-processed samples. Clearly the optimal morphology for energy conversion is not a true thermodynamic equilibrium morphology.

Energy-filtered TEM is a powerful technique for gaining insight into the extent of phase separation and purity of the phases in polythiophene/fullerene blends.[42-44] The electron energy loss spectra (EELS) of neat P3HT and $PC_{61}BM$ thin films are shown in Figure 2.4. The plasmon peak of neat P3HT occurs at approximately 23.4 eV, whereas that of neat $PC_{61}BM$ occurs at 26.0 eV. The shaded grey (19.4 ± 4 eV) and red (31.4 ± 4 eV) energy windows on the EELS spectra indicate the regions of strong inelastic scattering from P3HT and $PC_{61}BM$ component in the blend, respectively.

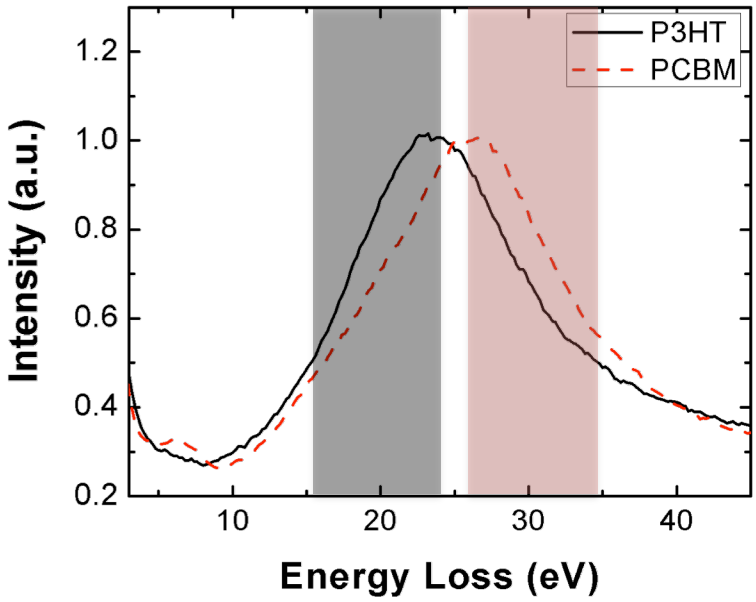

Figure 2.4 EELS spectra of neat P3HT, black line, and neat $PC_{61}BM$, red dashed line, for h=120 nm thick films are shown here. The red (to the right) and grey energy windows represent the energy loss regions where inelastic scattering is more intense from $PC_{61}BM$ and P3HT, respectively.

By selecting the corresponding energy window, the local elemental composition can be mapped due to significant differences in sulfur and carbon concentration between

P3HT and $PC_{61}BM$ respectively. Figure 2.5(a) – (c) shows the $PC_{61}BM$ maps in the bottom row of the EFTEM spectral images, the energy window has been selected so the $PC_{61}BM$ component appears bright and the P3HT component would appear dark. The image intensity is proportional to the concentration of each component; bright regions correspond to $PC_{61}BM$-rich while dark regions correspond to P3HT-rich domains. In the top row, the bright regions correspond to P3HT. We note that a certain degree of phase separation already occurred in the as-cast film consistent with the addition of nitrobenzene; see Figure 2.5(a).

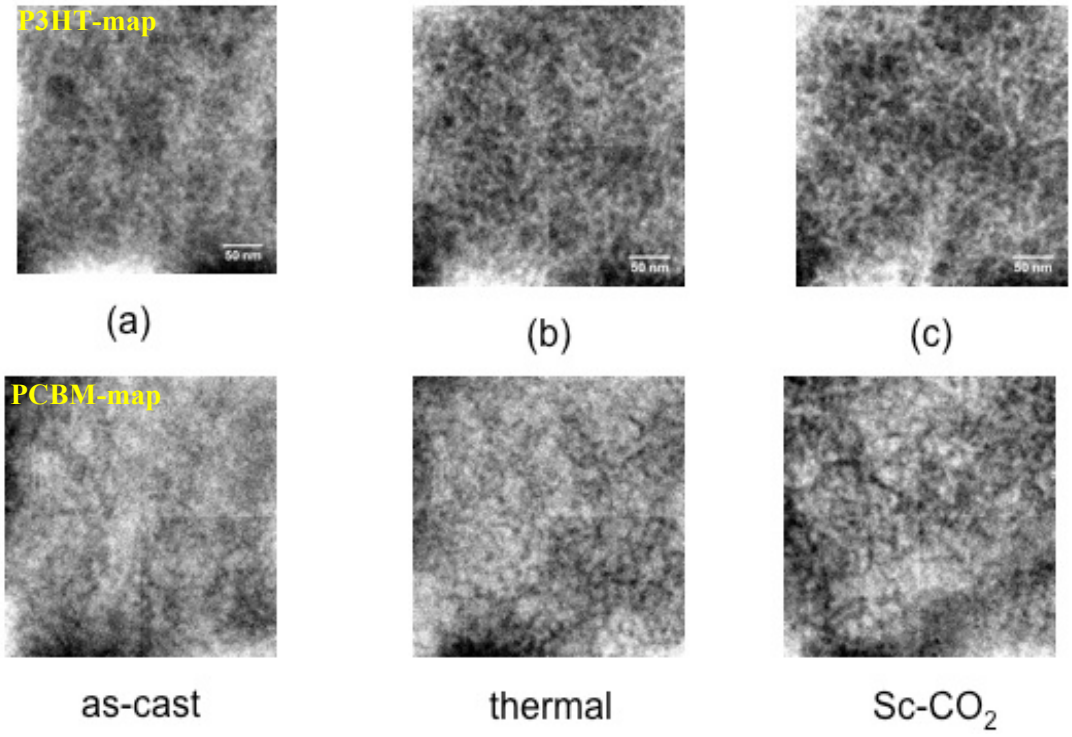

Figure 2.5 Energy filtered transmission electron microscopy (EFTEM) images P3HT:$PC_{61}BM$ spin cast from a 7 vol% nitrobenzene : chlorobenzene solution. In the top row, the energy window is selected so that $PC_{61}BM$ component is dark, and P3HT component is bright. (a), as-cast, (b), thermally annealed at 150 °C for 5 min, and (c) annealed in $scCO_2$ at 50 °C 10.34 MPa for 45 min. Shown in the bottom are the corresponding images where the P3HT regions appear dark and the $PC_{61}BM$ regions appear bright.

Thermal annealing enhanced phase separation, as shown in Figure 2.5(b) (top row); the P3HT-rich domains appear to be brighter than the as-cast sample. Annealing in $scCO_2$ at 50 ºC, 10.34 MPa, for 45 minutes promoted further phase separation between P3HT and $PC_{61}BM$ components, in Figure 2.5(c), also showing brighter P3HT-rich domains (top row) compared to the as-cast, but with similar nanoscale morphology to the thermal annealed. We note that the contrast window and level of all the images were the same.

We now provide quantitative information about the differences between the structures of the as-cast, the conventional high temperature processed, and the $scCO_2$ processed samples. While the optimal morphology for processing is not the true thermodynamic equilibrium P3HT/$PC_{61}BM$ morphology, it is a phase-separated structure of local regions of pure crystalline P3HT, pure $PC_{61}BM$ aggregates with amorphous phase-mixed P3HT/$PC_{61}BM$ regions.[17,18] The dimensions of the phases and molecular ordering may be reasonably optimized via controlling the phase separation kinetics that occurs upon heating at elevated temperatures, after the solvent-casting process.

Using EFTEM, we further examined the local phase purity of both P3HT-rich and $PC_{61}BM$-rich domains for each film. The plasmon peak positions of these regions averaged over 6 spectral images, chosen from random regions, for each sample are plotted in Figure 2.6. The dashed line indicates the plasmon peak of the 1:1 P3HT:$PC_{61}BM$ blend film on the EELS spectrum; see the spectral image in Figure 2.4, which is located between that of neat P3HT and neat $PC_{61}BM$, approximately at an energy of 24.6 eV. Clearly, the local plasmon peak positions deviate from the overall

average 24.6eV, implying that the local composition deviates from 1:1, as phase separation occurs between P3HT and $PC_{61}BM$.

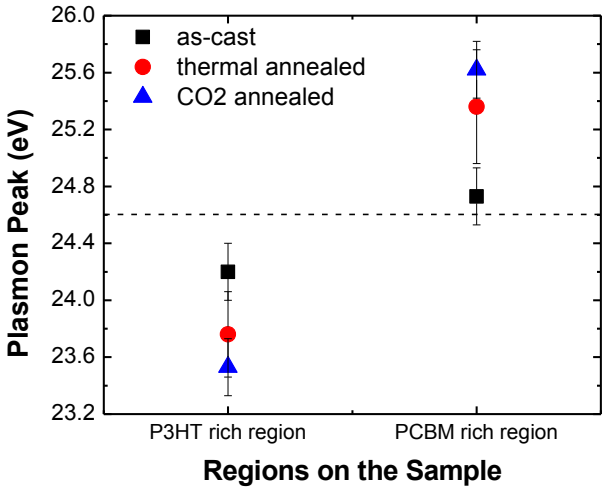

Figure 2.6 Plasmon peak positions of P3HT and $PC_{61}BM$ rich regions averaged over 6 EFTEM images of P3HT/$PC_{61}BM$ spin-coated from chlorobenzene with 7 vol% nitrobenzene. Square represents as-cast; circle, thermally annealed at 150 °C for 5 min, and triangle, annealed in $scCO_2$ at 50 °C, 10.34 MPa for 45 min.

The proximity of the plasmon peak position to the energy 24.6 eV is a measure of the degree of purity. As expected, the data indicate that the as-cast sample has the least phase separation; both P3HT-rich and $PC_{61}BM$-rich domains are close to the plasmon peak of the 1:1 blend. After thermal annealing, the phase separation between P3HT and $PC_{61}BM$ increased, as an average P3HT-rich domain peaked at 23.8 eV and $PC_{61}BM$-rich domain peaked at 25.4 eV, both deviated 0.8 eV from the overall average peak position. Samples processed using $scCO_2$ at 50 ^{o}C, 10.34 MPa for 45 min, exhibited the largest differences between the purities of the P3HT and $PC_{61}BM$ phases, without changes in domain size. The P3HT-rich domains exhibited an average plasmon peak at 23.6 eV and $PC_{61}BM$-rich domains at 25.6 eV, both 1 eV away from the overall average 24.6 eV.

These observations, associated with enhanced purity, are corroborated by uv-vis measurements of the samples. Figure 2.7 shows the normalized uv-vis absorption spectra illustrating the vibronic absorption peak and shoulders associated with P3HT π - π* transition, indicated by the green arrows. The intensity of the shoulder at 610 nm is more pronounced for the $scCO_2$-annealed sample at 50 ºC, 10.34 MPa for 45 min signifying a stronger inter-chain interaction and a higher degree of ordering and packing of P3HT polymer chains.[14,45]

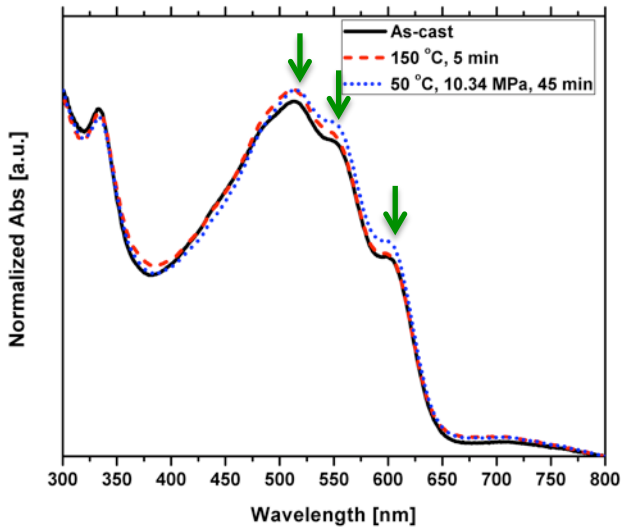

Figure 2.7 Uv-vis absorption normalized to the maxima of the spectra for P3HT/$PC_{61}BM$ blend prepared from chlorobenzene with 7vol% nitrobenzene, as-cast, thermal annealed at 150 ºC, 5 min, and $scCO_2$ annealed at 50 ºC, 10.34 MPa, 45 min.

These data clearly indicate the effectiveness of $scCO_2$ in enhancing phase purity, locally, compared to the as-cast samples. The data otherwise suggest that the phase purity of the thermal annealed and the $scCO_2$ annealed are comparable. It would be useful to begin with a discussion of well-known effects of $scCO_2$ on the morphology of polymers. Liquid and $scCO_2$ have emerged as environmentally benign alternatives to toxic organic solvents in polymer synthesis and processing such as foaming, plasticizing and

impregnation.[46-50] The sorption of CO_2 by polymers influenced by CO_2-polymer interactions has been shown to result in the swelling of soft penetrable surfaces leading to a plasticization effect, thereby increasing the free volume and chain mobility, which may promote significant registry of polymer chain orientations, facilitating mass transfer of solutes either into or out of the polymer phase.[47,51] Furthermore, the viscosity and diffusivity of $scCO_2$ relating to its density-dependent solvating power can be regulated with fine changes to pressure and/or temperature, making it appealing for controlling and fine-tuning the morphology of polymer thin films. Other studies have demonstrated the enhancement of polymer crystallization in the presence of $scCO_2$ and have also shown how the phase behavior of polymer-polymer mixtures is influenced by CO_2.[52-56] This is one of the primary reasons we have used this solvent for our study.

Having shown that, on average, the phases are comparable and the chain stacking is improved for the $scCO_2$ annealed sample at 50 ºC, 10.34 MPa for 45 min compared to thermally annealed at 150 ºC for 5 min, it is instructive to make a closer assessment of the local structure and nanoscale photoconductivity. Solvent-cast polymer based systems that undergo phase separation from the solvent generally lead to the formation of thin films with rough surfaces due to the phase formation process involving species with very different interfacial energies, attempting to form pure phases.[14,57] Here the composition varies locally in different locations throughout the sample, depending on the local film thickness. Analysis of the AFM data shows that the topography is composed of local maxima and minima; these data together with friction and phase contrast measurements indicate variations in local composition. The peak locations in the sample denote regions of high $PC_{61}BM$ concentration, based on AFM friction and phase contrast measurements.

The contrast in the friction is consistent with the relative differences between the average local compositions. The modulus and stiffness of $PC_{61}BM$ is higher than P3HT; the stiffness in the region of the peak locations posses higher stiffness indicating $PC_{61}BM$ aggregates. Note if the films are annealed for very long times, many hours, the $PC_{61}BM$ aggregates are visible optically.

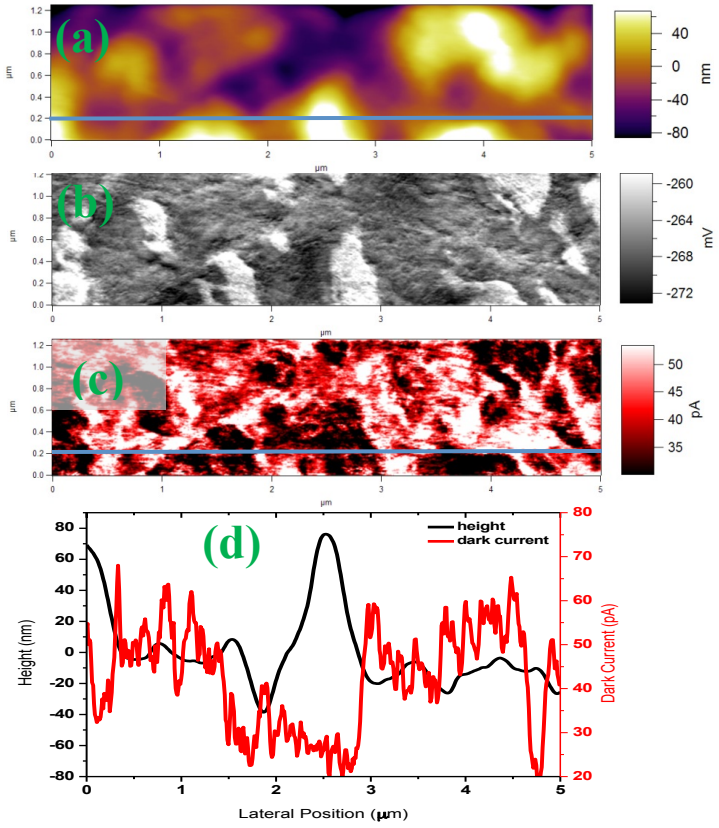

Figure 2.8 (a) Topographic map, (b) Friction map and (c) Corresponding dark current map for a bias of 1.2 V acquired for the P3HT/$PC_{61}BM$ blend cast from chlorobenzene with 7 vol% nitrobenzene and annealed at 50 ^{0}C and 10.34 MPa for 45min. (d) A dual cross section of the AFM images reveals variations in height (black line, left y-scale) and dark current (red line, right y-scale) along the same line in the topography and dark current images (blue line). AFM images are 5 μm x 1.2 μm.

In order to understand the role of the local composition of these regions we employed conductive AFM measurement using a Pt/Ir5 conductive cantilever. Due to the

high work function of both the ITO/PEDOT:PSS bottom electrode and Pt/Ir5 tip we expect a high energy barrier for electrons and ohmic contact for hole injection and thus measure the hole current and map the hole conduction network as already demonstrated by Ginger and co-workers and other groups.[58,59] Figure 2.8 shows topography, friction and dark current maps and the cross section of a line scan for the $scCO_2$ optimized sample annealed at 50 ºC, 10.34 MPa for 45 min. These data, at first glance suggest that the currents are associated with the topography of the sample. However this is misleading. We emphasize here that the small hole currents are measured in regions containing $PC_{61}BM$ aggregates. We note that for long annealing times, the aggregates increase in size, becoming visible optically, and the device performance is poor, due to the formation of a non-optimal composition. On the other hand, largest hole currents are associated with the donor P3HT-rich regions of the sample.

More importantly, we measured the local photocurrent at 0 V bias using pcAFM where a 532 nm laser was used to illuminate the sample at an intensity of ~10^4 W/m^2. Figure 2.9(c) shows the cross-section of a line scan for the sample annealed at 50 ºC, 10.34 MPa for 45 min. It is clear the P3HT-rich 'valleys' correspond to regions of higher photocurrent. The regions of $PC_{61}BM$ aggregates exhibited low photocurrent. It has been shown that this is to be expected due to a significant amount of recombination of carriers and the fact that the P3HT phases are mixed with $PC_{61}BM$ at such compositions.[60]

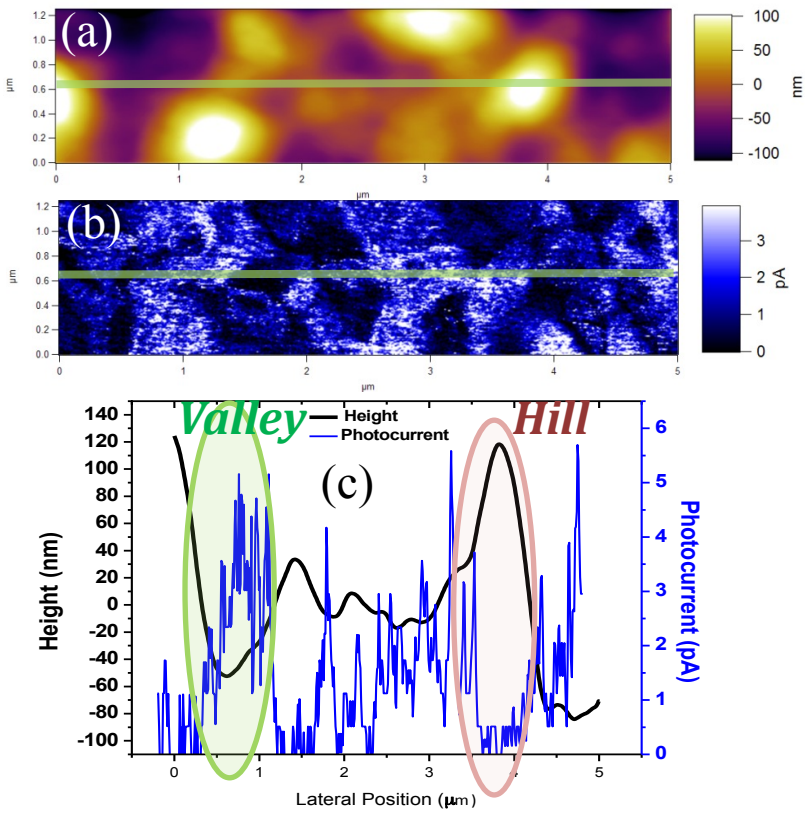

Figure 2.9 AFM topographic and photoconductivity image of the film processed at T=50 ºC and P=10.34 MPa for 45min. (a) Topography, (b) Corresponding photocurrent map and (c) A dual cross section indicating variations in height (black line, left y-scale) and photocurrent (blue line, right y-scale) along the line drawn in part (a) and part (b) of the sample. AFM images are 5 μm x 1.2 μm.

The AFM photocurrent maps provide some insight into the differences between the macroscopic performance of the devices, processed using different strategies. The images in Figure 2.10 reveal that the sample processed at 50 ºC, 10.34 MPa, for 45 min using $scCO_2$ possessed a larger area of regions that exhibited photoconductivity. This observation may be quantified by integrating over the areas that exhibited photocurrents to obtain a current density. With regard to the $scCO_2$-annealed sample that exhibited the best efficiency, this was 10.27 $nA/\mu m^2$; it was 3.77 $nA/\mu m^2$ for the as-cast sample and 5.94 $nA/\mu m^2$ for the thermal annealed sample. In the case of one other $scCO_2$-processed

sample that exhibited a lower PCE and J_{SC}, the value was 4.27 nA/μm^2. This can be further quantified in terms of percent (%) of active area, which is 35% for as-cast, 32% for the thermal annealed and 79% for the optimized $scCO_2$ annealed sample.

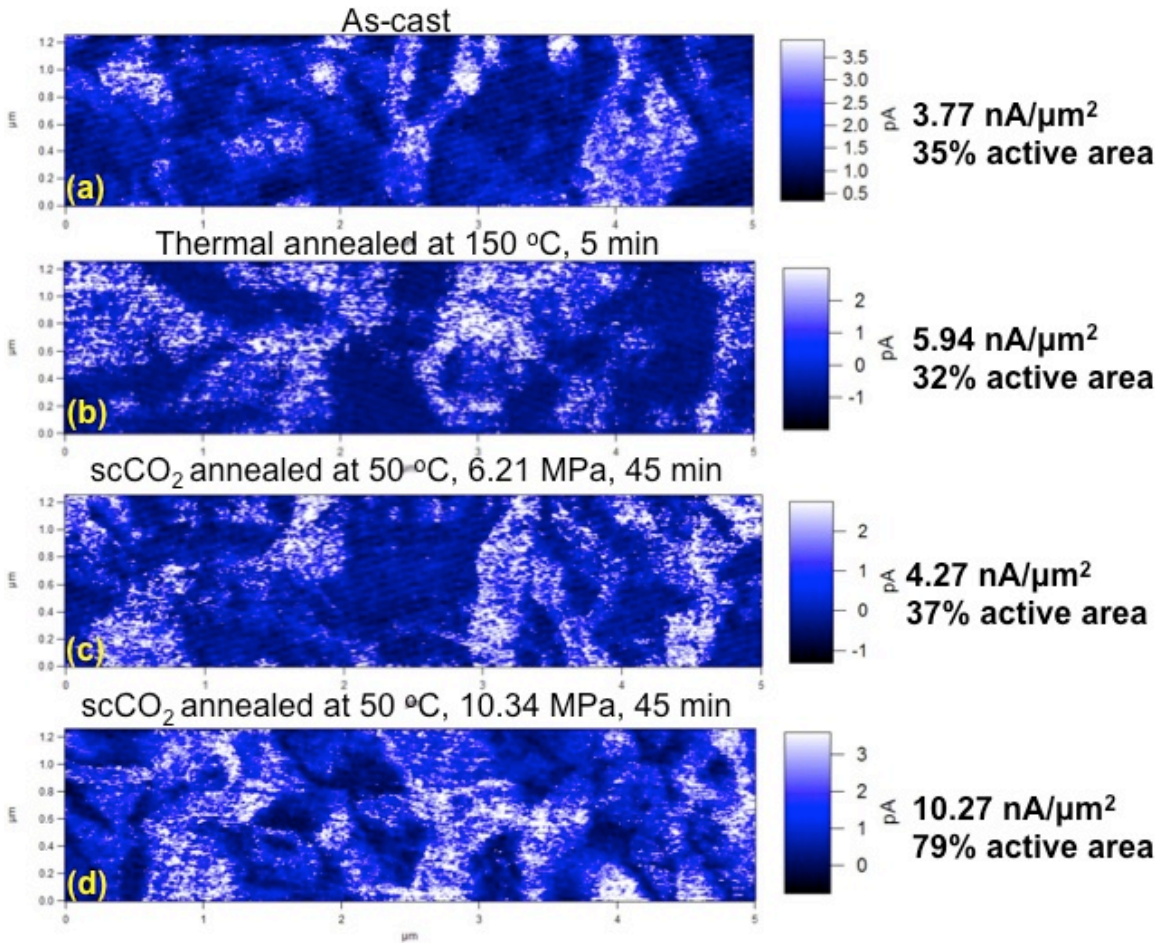

Figure 2.10 Photocurrent maps of (a) as-cast, (b) thermal annealed, 150 ºC, 5 min and (c) $scCO_2$ annealed at 50 ºC, 6.21 MPa, 45 min and (d) $scCO_2$ annealed at 50 ºC, 10.34 MPa, 45 min. AFM images are 5 μm x 1.2 μm.

It is evident from these studies that the main effect of the supercritical solvent is to improve the local phase purity, and hence intermolecular interactions and local crystallinity. Processing has the effect of improving the efficiency of a larger fraction of

active regions of the sample, as manifested by the pcAFM studies (Figure 2.10), and quantified in Figure 2.11.

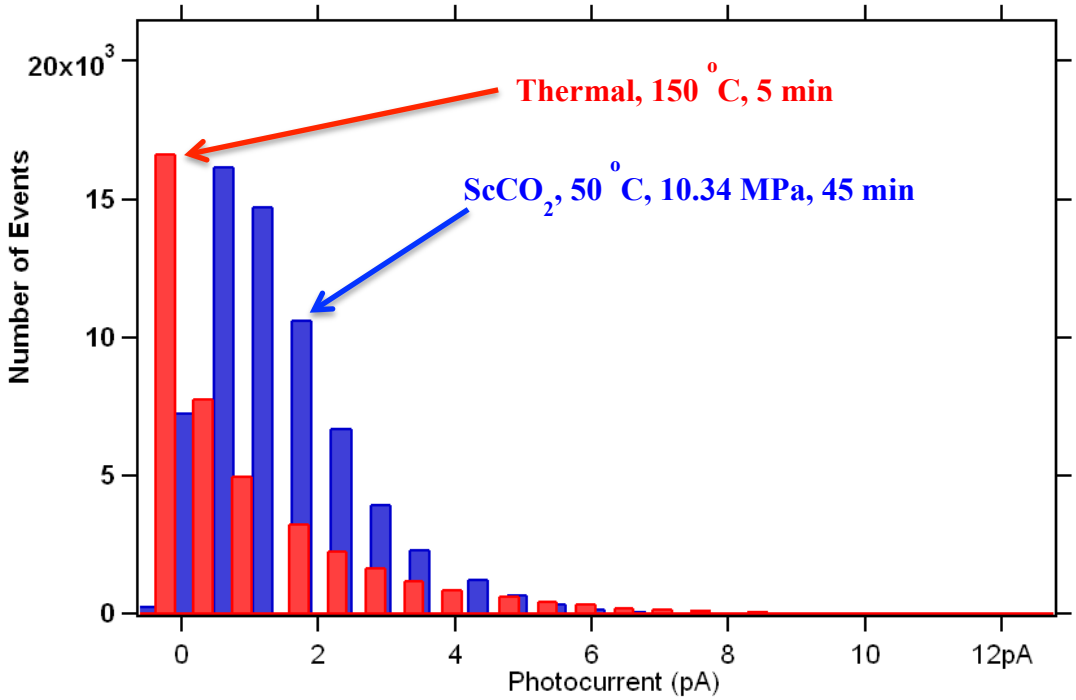

Figure 2.11 Histograms of photocurrent maps of samples thermal annealed, 150 ºC, 5 min and $scCO_2$ annealed at 50 ºC, 10.34 MPa, 45 min.

Since, to first order, the V_{OC}, determined by the difference between HOMO level of the donor and LUMO level of the acceptor, and the FFs, are comparable for all the processed samples, then the change in the PCE of the device is largely dictated primarily by changes in the J_{SC}. The reduction in the extent of phase mixing of an as-cast, phase mixed, sample has a number of effects on the device performance. It increases the effective D/A area, A_{intf}, which enables a larger number of excitons to reach the D/A interface with a reduction in geminate recombination. The efficiency of the production of free carriers at the D/A interface, is sensitive to the interfacial structure.[61,62] Processing leads to sharper interfaces, necessarily associated with increased phase separation, and

increased order. However, continued processing leads to a reduction in A_{intf} and a reduction, necessarily, in the number of pathways that lead to the electrodes; this leads to a reduction in J_{SC}. Note that the PCBM-rich regions (randomly located throughout the film), which increase in size, are responsible for the reduction in A_{intf}, thereby reducing the active device areas, as shown from the pcAFM data. This is responsible for an overall reduction in J_{SC}. Clearly, the local efficiencies of regions throughout the sample are reduced because the local compositions are not optimal. One primary advantage of $scCO_2$ is that it has a mild effect on the structure of the sample, making it possible to achieve greater control over the nanoscale structure by varying the temperature and pressure compared to the aggressive high temperature process.

2.4 Conclusions

We proposed an alternative protocol using a supercritical fluid, $scCO_2$, to fabricate bulk heterojunction photovoltaic devices. By controlling the pressure, temperature and density of the supercritical fluid, the performance of a P3HT/PC_{61}BM solar cell, J_{SC}s and PCEs, was comparable to and in some cases better than devices processed using the conventional high temperature thermal annealing protocol. In devices that yielded the best PCEs and J_{SC}s, energy-filtered TEM uv-vis measurements studies reveal that the phase purities of P3HT-rich and PC_{61}BM-rich domains are highest compared to as-cast and comparable to thermally annealed blends. A larger fraction of regions that exhibit photoconductivity was associated with improved device efficiency. The lowest active device areas, and most phase mixed regions, were exhibited by the as-cast samples. Our work points out that low temperature $scCO_2$ annealing can be used as a general strategy to promote optimal phase separation, and purity, between the donor

and acceptor of polymer bulk heterojunction solar cells. It is a mildly plasticizing solvent, which has a preferential affinity for one component and furthermore promotes nanoscale, not macro-scale, phase separation, necessary to improve the device efficiency compared to the higher temperature thermal annealing where active components start to degrade after a rather short time.

CHAPTER 3:

An All-Conjugated Gradient Copolymer Approach for Morphological Control of Polymer Solar Cells

J.A. Amonoo, A. Li, G. E. Purdum, M. E. Sykes, B. Huang, E. F. Palermo, A. J. McNeil, M. Shtein, Y-L. Loo and P. F. Green *J. Mater. Chem. A, 2015, 3, 20174–20184*

3.1 Introduction

Conjugated polymer:fullerene bulk-heterojunction (BHJ) systems offer a low-cost avenue to flexible thin-film solar cell technology. The overall device performance is inextricably linked to the three-dimensional molecular arrangement of the active materials; nanoscale morphology plays a critical role in the exciton dissociation and charge transport processes. For a particular blend system, improvement in power conversion efficiency (PCE) is typically achieved by controlling phase-separation length scales using post-production protocols (annealing) or high boiling-point solvent additives.[34,63] The optimum nanoscale morphology consists of donor/acceptor (D/A) domains on the order of the exciton diffusion length (~10 nm), and large interfacial area in the bulk associated with D/A phases forming percolated networks facilitating charge

separation and transport.[64] This putatively ideal morphology is not the true thermodynamic equilibrium morphology, but rather a kinetically trapped metastable structure. Hence, polymer solar cell device performance generally degrades upon extended processing or aging as the system approaches a more stable, and less favorable, morphology unless a compatiblizer is introduced to arrest the kinetically trapped morphology.[65,66] For the extensively studied P3HT:PCBM system, prolonged processing increases the domain size of the fullerene aggregates, leading to a reduction in D/A interfacial area and ultimately reduces PCE.[67]

For this reason, significant research has been geared towards improving the long-term thermal stability of polymeric solar cells. The active layer microstructure is often described as a combination of ordered polymer-rich domains, fullerene-rich aggregates and mixtures of molecularly dispersed fullerene in disordered polymer regions.[68] Most of the efforts to improve thermal stability have focused on suppressing phase separation and stabilizing polymer/fullerene interfaces in the active layer using photo-crosslinkable conjugated polymers,[69] thermally stable copolymers,[70-72] copolymer and molecular additives as suitable compatibilizers[65,66,73] and donor polymers low in regioregularity.[74]

Recently, the use of rod-rod π-conjugated copolymers in BHJ polymeric solar cells as either the primary donor material or additives serving as nanostructuring agents has garnered significant interest as an effective method to control nanoscale morphology, promote phase separation, and improve thermal stability.[72,75,76] However, none of these has included the use of fully π-conjugated gradient sequence copolymers as the main donor species. Besides their inherent ability to self-assemble into well-defined nanostructures, copolymers offer the additional advantage of fine-tuning physicochemical

properties through advanced synthetic chemistry of the constituent molecules, thus providing opportunities for further improvement. While methods for synthesizing coil-coil gradient copolymers with precise composition profiles have existed,[77,78] it is only recently that nickel-catalyzed "living" chain growth polycondensation techniques have enabled exquisite control of the copolymer chain architecture and comonomer sequence distribution of π-conjugated systems.[79-81] For example, π-conjugated gradient copolymers, whose instantaneous composition varies gradually along the polymer chain (Figure 3.1), are now accessible by these emerging methods.[81-84]

Gradient copolymers exhibit a unique set of physical and morphological properties generally intermediary between that of the block copolymer (Figure 3.1), which possesses a step change in composition, and the random copolymer, which possesses a uniform composition profile along the polymer chain.[66,85-87] Furthermore, gradient copolymers have been shown to be effective interfacial modifiers, offering a larger degree of control over the interfacial profile in polymer blends.[88] Gradient copolymers have numerous uses spanning applications as blend compatibilizers,[88,89] damping materials,[90] and thermoplastic elastomers.[91] Recently, π-conjugated gradient copolymers containing 3-hexyl selenophene (3HS) and 3-hexyl thiophene (3HT) units were introduced and it was found that poly(3-hexylselenophene-*gradient*-3-hexylthiophene) P(3HS-*g*-3HT) displayed distinctive physical, optical and thermal properties compared to the block, poly(3-hexylselenophene-*block*-3-hexylthiophene) P(3HS-*b*-3HT), and random poly(3-hexylselenophene-*random*-3-hexylthiophene) P(3HS-*r*-3HT) analogs.[82]

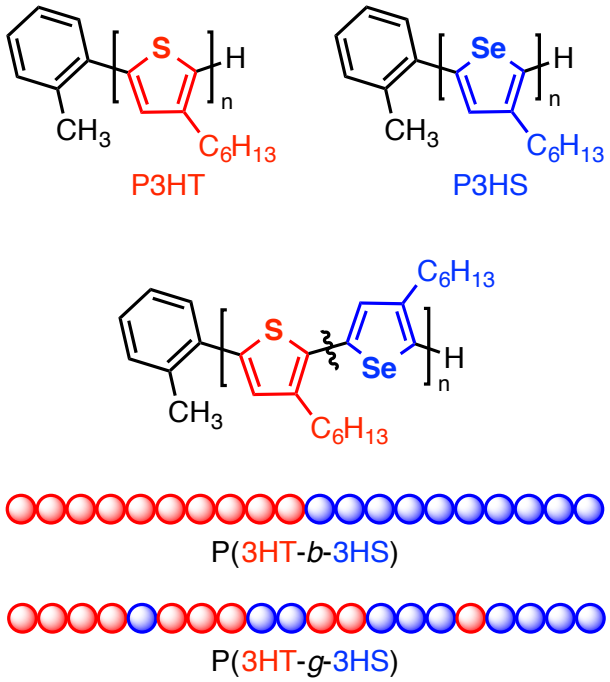

Figure 3.1 Chemical structure of the polymers and copolymers used in this work.

In this study, to gain a deeper understanding into the role of molecular sequence along the copolymer chain and structure-property-performance relationships of π-conjugated copolymers, we evaluate the nanoscale morphology, thermal stability and device performance of P(3HS-*g*-3HT) and P(3HS-*b*-3HT) as donor materials in polymer:fullerene photovoltaic systems. From energy-filtered transmission electron microscopy (EFTEM) measurements, the gradient copolymer device shows a continuous interconnected fibril network relative to the block architecture, suggesting a larger interfacial area in the bulk between the polymer and fullerene components. This result is further corroborated by carrier dynamics measurements using photo-CELIV where we found that the gradient copolymer device generated the highest initial carrier density. Furthermore, an accelerated degradation test revealed the gradient copolymer device to

be the most robust, maintaining the highest optimum performance with prolonged annealing.

3.2 Results and Discussion

The P(3HS-*g*-3HT) and P(3HS-*b*-3HT) copolymers used in this study were synthesized and characterized using previously published procedures (see supporting information for details).[82] Figure 3.1 shows the chemical structure of the homopolymers and copolymers with a schematic of the copolymer chain architecture. In the gradient design, the block-like chain ends are covalently linked by a gradual change in comonomer composition along the copolymer chain. A physical blend of the two homopolymers (P3HS:P3HT) in a 1:1 mass ratio was used for comparison to elucidate the importance of molecular ordering along the polymer chain. The molecular weight distributions, number-average molecular weights and regioregularity of all polymers used were nearly identical to isolate the effect of copolymer chain sequence, see Table 3-1 Summary of chemical information. For the copolymers, molar compositions of the comonomers were approximately 1:1. Devices were fabricated in the inverted device architecture for stability under ambient conditions.[92]

Polymer	Mn (kDa)	Đ	% Selenophene	Regioregularity (%)
P3HT	31.2	1.18	0	97
P3HS	23.4	1.21	100	98
P(3HS-*b*-3HT)	26.2	1.14	50	97
P(3HS-*g*-3HT)	32.6	1.18	50	97

Table 3-1 Summary of chemical information

3.2.1 Absorption Spectra of Thin Films and Device Spectral Response

We first studied the photophysical properties of the optimized polymer:fullerene blends using UV-visible spectroscopy. Figure 3.2 UV-vis absorption spectra of optimized samples of P3HT:PCBM (red), P3HS:PCBM (blue), P3HS:P3HT:(1:1)PCBM (dark yellow), P(3HS-*b*-3HT):PCBM (black) and P(3HS-*g*-3HT):PCBM (green). shows the normalized absorption spectra where the wavelength range is selected to highlight the absorption profile of the polymers. We found that P3HS absorption is significantly red-shifted from that of P3HT, consistent with other studies and the fact that P3HS has a lower band gap.[93,94] Both P3HT and P3HS polymers show characteristic vibronic structures manifested as strong absorption shoulders near 610 nm and 700 nm respectively, associated with π-aggregation and strong interchain interaction.[14,94] The P(3HS-*b*-3HT) copolymer showed an almost identical absorption profile to the homopolymer blends of P3HS:P3HT (1:1) suggesting the existence of phase separation between the P3HS-block and P3HT-block in the block copolymer[95] and that P3HS and P3HT are thermodynamically incompatible and immiscible. For the P(3HS-*g*-3HT), we observed weak absorption features associated with 3HT and 3HS chain interaction at 610 nm and 700 nm. This apparent reduction of π-aggregation in the P(3HS-*g*-3HT):PCBM films suggests that, relative to the block copolymer, the composition gradient along the polymer chains disrupts the thiophene-thiophene and selenophene-selenophene π-interactions and that alignment and packing may be constrained to the chain termini. This was the same in the annealed neat P(3HS-*g*-3HT) film (not shown here).

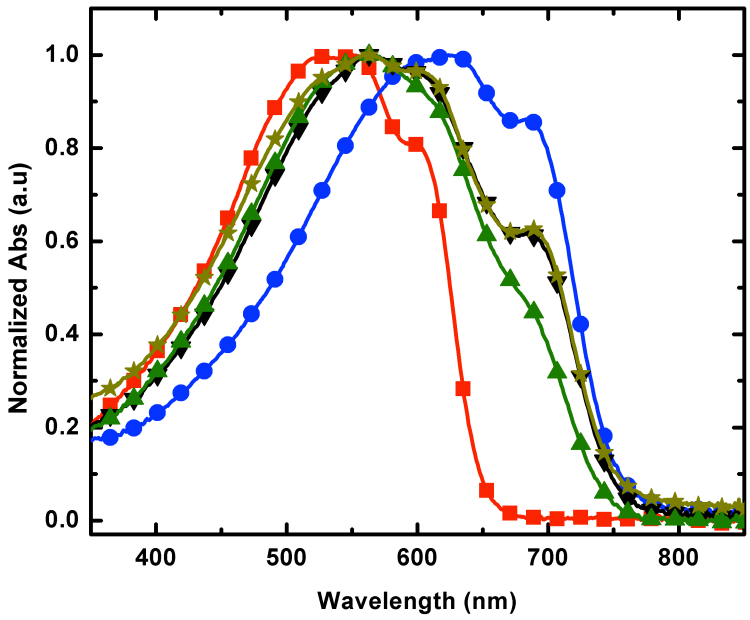

Figure 3.2 UV-vis absorption spectra of optimized samples of P3HT:PCBM (red), P3HS:PCBM (blue), P3HS:P3HT:(1:1)PCBM (dark yellow), P(3HS-*b*-3HT):PCBM (black) and P(3HS-*g*-3HT):PCBM (green).

External quantum efficiency (EQE) measurements were performed and compared to the absorption profiles. EQE plots are shown in Figure 3.3. We note that even though the absorption spectra of P(3HS-*b*-3HT) and the 1:1 blend are almost identical, their spectral response is very dissimilar both in the P3HT (400 nm – 650 nm) and non-P3HT absorbing regions (650 nm – 750 nm). The data shows that photon harvesting is decreased in both P3HT-block and P3HS-blocks in P(3HS-*b*-3HT):PCBM device. Even though the copolymers have comparable comonomer molar compositions, interestingly, the intensity of the EQE spectra of P(3HS-*g*-3HT):PCBM and P(3HS-*b*-3HT):PCBM vary markedly in the P3HT absorbing region but are similar in the 650 nm - 750 nm wavelength range. These results suggest the composition gradient in the polymer donor improves photon harvesting in the P3HT absorbing region.

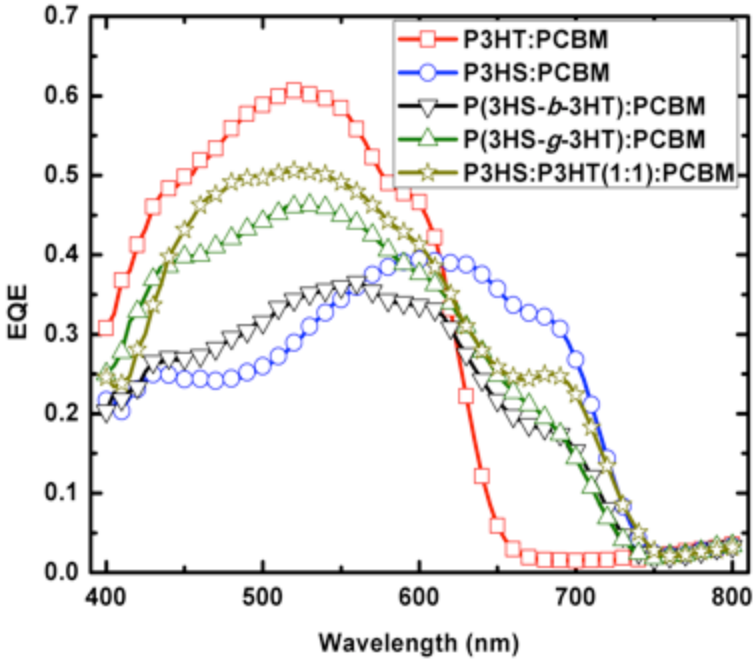

Figure 3.3 External quantum efficiency spectra of optimized devices of P3HT:PCBM (red square), P3HS:PCBM (blue circle), P3HS:P3HT:(1:1)PCBM (dark yellow star), P(3HS-*b*-3HT):PCBM (black triangle) and P(3HS-*g*-3HT):PCBM (green triangle).

3.2.2 Bulk Heterojunction Device Performance and Thermal Stability

Having shown that the optical properties of the homopolymers can be tailored by finely adjusting the copolymer sequence, we proceed to evaluate their performance in photovoltaic devices. Each polymer:fullerene device was optimized independently, especially with regards to weight fraction of the active materials and fabrication procedure. For the gradient and block copolymers, the optimum copolymer:fullerene ratio was the same at 55:45. Details can be found in the methods section. Representative J-V curves under 1-sun simulated solar illumination display typical diode-like behavior as shown in Figure 3.4. For all optimized devices, P3HT:PCBM was still the "champion" (3.7 ± 0.1%). Interestingly, the P(3HS-*g*-3HT):PCBM device performed reasonably well

(3.3 ± 0.1%), whereas the P(3HS-*b*-3HT):PCBM and P3HS:PCBM devices were less efficient.

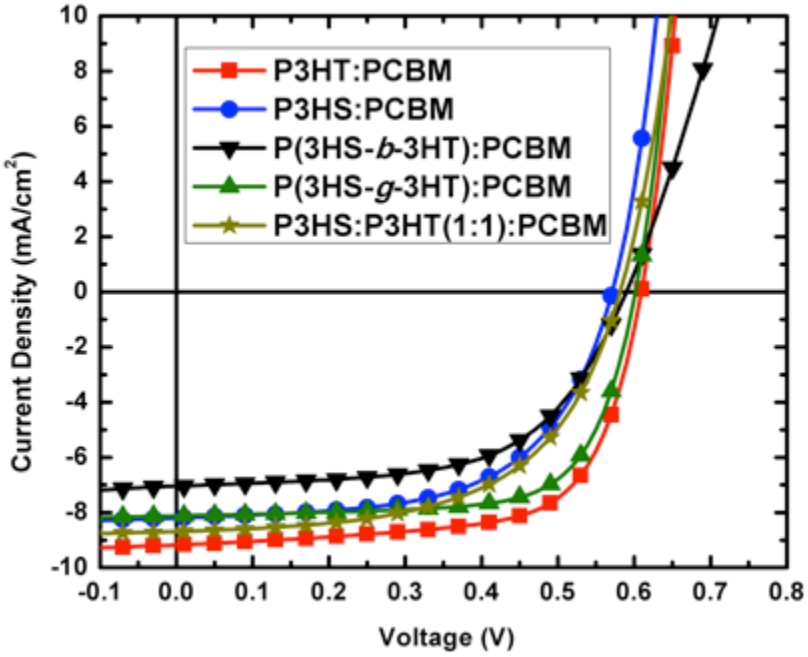

Figure 3.4 Current density-Voltage (J-V) curves of optimized devices of P3HT:PCBM (red square), P3HS:PCBM (blue circle), P3HS:P3HT:(1:1)PCBM (dark yellow star), P(3HS-*b*-3HT):PCBM (black triangle) and P(3HS-*g*-3HT):PCBM (green triangle).

We then designed a series of thermal stability experiments to further understand the relationship between the active layer microstructure and performance. The evolutions of the PCE, short circuit current density (J_{SC}), open circuit voltage (V_{OC}) and fill factor (*FF*) as a function of annealing time at 150 ^{o}C are highlighted in Figure 3.5.

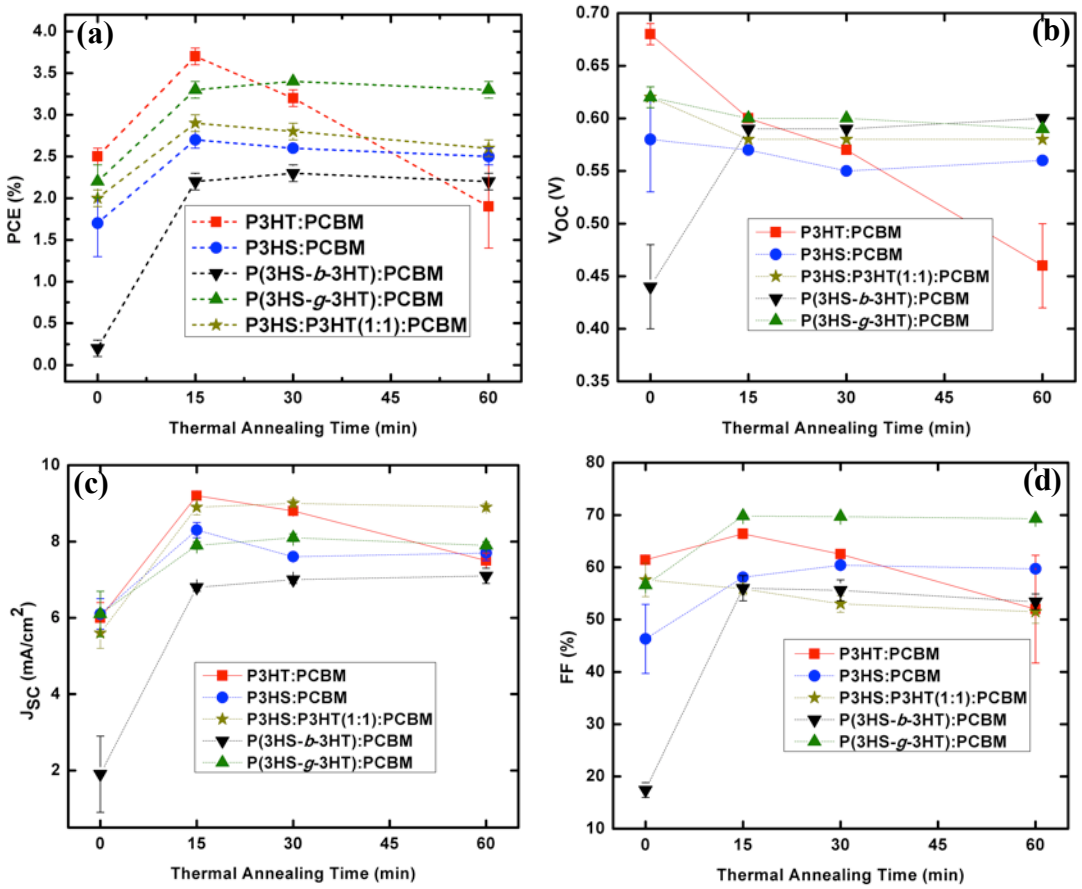

Figure 3.5 Plots of (a) PCE (b) V_{OC} (c) J_{SC} and (d) *FF* as a function of annealing time at 150 °C for P3HT:PCBM (red square), P3HS:PCBM (blue circle), P3HS:P3HT:(1:1)PCBM (dark yellow star), P(3HS-*b*-3HT):PCBM (black triangle) and P(3HS-*g*-3HT):PCBM (green triangle).

We will discuss the V_{OC} trend in relation to charge carrier decay dynamics later. For each materials pair, at least 9 devices were measured, yielding the error bars in the figure. We clearly see that all P3HS-based devices demonstrate superior thermal stability over long annealing times in contrast to the P3HT-only device, which steadily declines in performance after reaching a maximum after 15 min. Previous studies of P3HS:fullerene mixtures have shown that during thermal treatment, there exists a higher fraction of disordered polymer phase in P3HS:PCBM films even though P3HS packs much better and forms high quality crystallites relative to P3HT in P3HT:PCBM blends.[96] This tends

to facilitate the mixing of PCBM molecules with P3HS and thereby suppress PCBM aggregation.[96] This is in contrast to the P3HT:PCBM system where phase separation continues with annealing leading to lower PCE, as shown in Figure 3.5(a). The most straightforward explanation is that the 3HS components become more miscible with PCBM upon thermal annealing, stabilizing the morphology and preventing further phase separation. It is also noteworthy that the melting temperature (T_m) of P3HT ($T_{m,\ P3HT}$ = 243 ^{o}C) is lower than that of P3HS ($T_{m,\ P3HS}$ = 256 ^{o}C)[82], which possibly reflects differences in chain mobility at the annealing temperature. These results demonstrate that the composition gradient along the copolymer chain in the P(3HS-*g*-3HT):PCBM offers the morphology that stabilizes the D/A interface while simultaneously providing the optimum nanostructure required for charge separation and collection.

3.2.3 Polymer Crystallization: GIXD

We employed grazing-incidence X-ray diffraction (GIXD) to probe the long-range intermolecular order and crystallinity of the optimized polymer:fullerene samples. The two-dimensional GIXD patterns and the normalized intensity traces taken at qxy = 0 associated with the polymer donors in the samples are shown in Figure 3.6. The GIXD patterns clearly show that the homopolymers, blends, and copolymers all self-organize into periodic lamellar structures; that the intensities of the (h00) reflections of P3HT and P3HS are concentrated along the meridian indicates that the polymer crystallites are preferentially oriented in an edge-on fashion.[97] Taking a line cut of the two-dimensional GIXD patterns at qxy = 0 yields one-dimensional X-ray trace representative of the out-of-plane reflections (Figure 3.6f and Figure 3.6g). The traces associated with the P3HT and P3HS homopolymers reveal the (100) reflections at 0.38 Å-1 and 0.41 Å-1, respectively,

consistent with a prior report.[98,99] The line trace of the film comprising a blend of both P3HT and P3HS reveal reflections associated with both polymer donor constituents, as seen most clearly by distinct (200) reflections (Figure 3.6g). Interestingly, the GIXD images of both the block and gradient copolymers also reveal evidence of coexistence of crystallites of both polymer donor constituents; this can be best seen in the vertical line traces of the (200) reflections in Figure 3.6g in which the x-ray intensities in this q-range can be fitted to two Gaussians with centers corresponding to the (200) reflections associated with P3HT and P3HS homopolymers. The fractional intensities corresponding to each Gaussian can thus be used as a proxy for the relative crystallinity of 3HS and 3HT, and obtain a relative measure of the lamellar packing order. Carrying out this analysis reveals that, of the crystalline portions of the 1:1 blend and copolymer films, only 10-20% can be attributed to 3HT. This analysis suggests that for all annealed samples, the 3HS components exhibit enhanced fractional crystallinity related to the packing order of the lamellar compared to the 3HT segments within the homopolymer blend and copolymer films with PCBM. In other words, the 3HS crystalline phase comprises of higher quality crystals of enhanced lamellar packing order than the 3HT crystalline phase.

Recent studies have shown that in an all-conjugated block copolymer system, phase separation is induced by the identity of the heterocycle.[95] Even though the exact interaction between the two blocks during crystallization is not yet well understood, it has been suggested that in these highly rigid-rod-like block copolymers, the first block to crystallize would be the one with the highest T_m.[100] In this instance, the microphase-separated structure would be dictated by this block, which could confine the crystallite

size and domains of the other block. Since $T_{m,\ P3HT} < T_{m,\ P3HS}$ we can thus reasonably infer that the 3HS block/segment is likely to initiate crystallization of the copolymer, and as a result, further constrain the crystallization of the covalently-bound 3HT block/segments. Consequently, differences in the spatial arrangements and locations of 3HS components along the copolymer chain influence the crystallization behaviour leading to differences in nanoscale morphology as will be discussed in the following section.

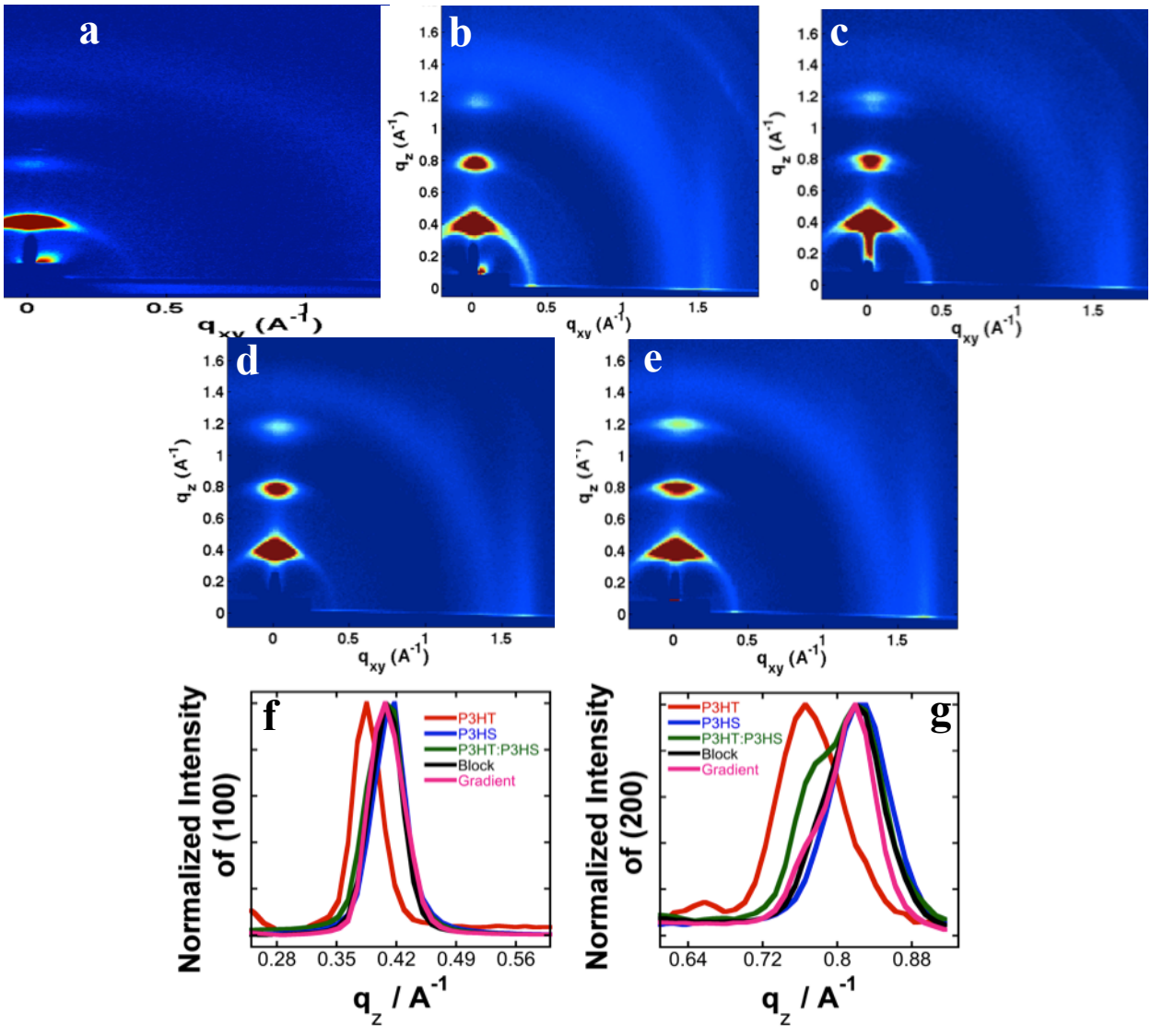

Figure 3.6 Grazing Incidence X-ray Diffraction (GIXRD) patterns of optimum samples of (a) P3HT:PCBM (b) P3HS:PCBM (c) P3HS:P3HT:(1:1)PCBM), and (d) P(3HS-*b*-3HT):PCBM, (e) P(3HS-*g*-3HT):PCBM. Normalized intensity traces taken at $q_{xy} = 0$, indicative of the (100) and (200) reflections (f and g, respectively).

3.2.4 Active-Layer Morphology Characterization: EFTEM

The nanoscale morphology of the optimized polymer:fullerene samples was studied using energy-filtered transmission electron microscopy (EFTEM) to distinguish between polymer and fullerene-rich phases.[43] After taking the spectral images, an energy-loss window was selected to maximize contrast in scattering intensity between the phases; the images in Figure 3.7 were integrated over the energy-loss range of 31.5 ± 3 eV such that the PCBM-rich regions appear bright and the polymer fibrils/domains appear dark. A qualitative comparison between the P(3HS-*b*-3HT):PCBM and P(3HS-*g*-3HT):PCBM samples reveals that the gradient copolymer forms a more uniform and continuous network of polymer fibrils within the fullerene-rich phase, which would be associated with facile carrier transport and a large D/A interface for exciton dissociation. On the other hand, the fibrils formed by the block copolymer assemble into dense clusters separated by large fullerene-rich regions with sparse fibrils. This type of meso-scale organization suggests a smaller D/A interfacial area and fewer continuous pathways for hole transport. Furthermore, this result shows that the gradient architecture tends to mitigate the intrinsic self-assembly characteristic of its block copolymer analog. One way to explain this observation is to first recall that the gradient sequence disrupts the strong interaction between 3HS and 3HT components in the block architecture, with 3HS being the precursor for the copolymer crystallization process. For the gradient copolymer, inter-chain π-interactions between selenophene-selenophene segments are restricted to the chain ends, which are block-like (see Figure 3.1). Additionally, the gradual change in

composition along the chain results in a weaker interaction between the segments near the chain centre, resulting in an inhibition in self-assembly for the gradient copolymer in comparison with the block copolymer, as shown. A similar effect was reported in recent work by Seferos and co-workers of the statistical variant, P(3HS-*s*-3HT), in which the statistical distribution of the comonomers along the chain were shown to interrupt the strong interaction between 3HS components leading to improved solubility and an extreme reduction in structural order relative to the block copolymer.[101] With regards to our results, it is evident that the gradient copolymer provides morphological characteristics that are intermediate between the statistical copolymer, where vapor annealing is required to improve the nanoscale order, and the block copolymer, which undergoes intrinsic phase separation.

In addition, simulations of the micro-phase separation characteristics of gradient and symmetric block copolymer thin films that form lamellae have shown that the physics of self-assembly between the two systems are fundamentally different even for the same lamellar period.[102,103] For linear gradient copolymers, variations in composition along the chain results in an A-B monomer interaction that drives A-rich and B-rich chain termini from the comonomers at the relatively broad region of the chain centre.[102] In contrast, for the block copolymer, the A-B monomer interfacial regions are localized to the narrow interface of the chain junction.[102] A natural occurrence of the structure is that, at very high χN, gradient copolymers exhibit much weaker phase segregation relative to their block copolymer counterparts which possess a much narrower interfacial region.[103] These simulations are consistent with our EFTEM studies; the strong and weaker interaction between the chain ends and centre respectively tends to influence the

crystallization behaviour which increases the interfacial area between the gradient copolymer and fullerene resulting in a higher D/A interfacial area and in the process generated the highest initial carrier density which will be discussed in the next section. Because, the block copolymer device exhibited a stronger tendency to phase segregate, leading to less D/A interfacial area, the lowest initial carrier densities were measured. Although it is not obvious at the scale/resolution of images in Figure 3.7, the P3HT:PCBM sample possesses finer fibrillar features than the copolymers (see Supporting Information for higher magnification image). The P3HS:P3HT:PCBM blend shows large and poorly-defined "patches" of polymer-rich/fullerene-rich regions, consistent with the existence of phase-separated "domains" of P3HS:PCBM and P3HT:PCBM.

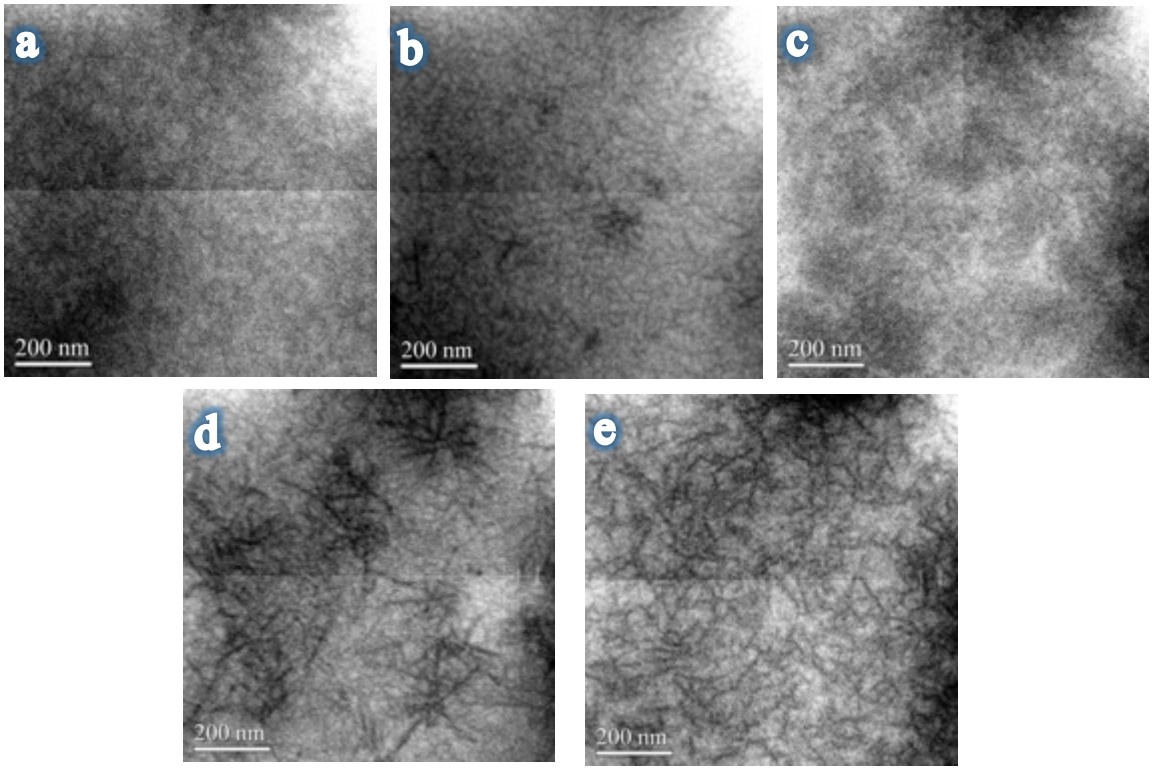

Figure 3.7 Energy-filtered transmission electron microscopy (EFTEM) images of (a) P3HT:PCBM (b) P3HS:PCBM (c) P3HS:P3HT:(1:1)PCBM), and (d) P(3HS-*b*-3HT):PCBM and (e) P(3HS-*g*-3HT):PCBM. The energy window is selected such that the polymer-rich phase is dark.

3.2.5 Carrier Dynamics

To gain information about carrier generation and recombination, devices were characterized using photo-CELIV. In this technique, the transient current generated by a 532 nm laser pulse excitation is measured at various delay times and a linearly increasing voltage applied to extract the carriers yielding a photo-generated carrier density. Figure 3.8 shows plots of charge carrier density versus delay time for optimum devices studied. All devices showed a decrease in carrier density as delay time increased reminiscent of recombination in the active layer. Since the curves exhibit a power law dependence with

time, $n(t) \propto t^{\alpha}$, we fit the data sets to the power law formula and extrapolated to t=0 to obtain the initial carrier density n(0), for each device. The data obtained is as follows: P3HT:PCBM, $n(0) = (1.34 \pm 0.3) \times 10^{17}$ cm^{-3}, P3HS:PCBM, $n(0) = (1.48 \pm 0.3) \times 10^{17}$ cm^{-3}, P(3HS-*b*-3HT):PCBM, $n(0) = (5.54 \pm 0.3) \times 10^{16}$ cm^{-3}, and P(3HS-*g*-3HT):PCBM, $n(0) = (3.92 \pm 0.3) \times 10^{18}$ cm^{-3}.

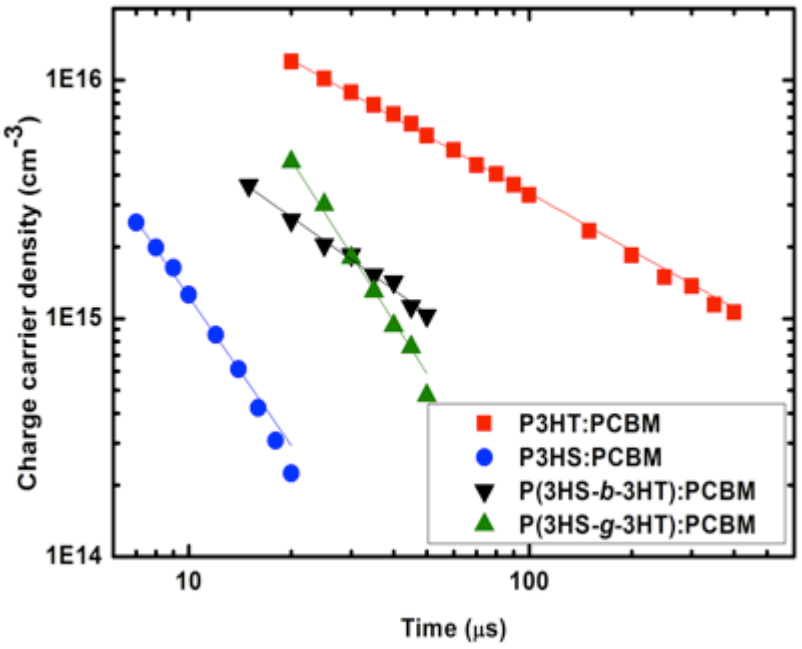

Figure 3.8 Concentration of extracted photogenerated charge carriers as a function of delay time measured by photo-CELIV for optimized devices of P3HT:PCBM (red square), P3HS:PCBM (blue circle), P(3HS-*b*-3HT):PCBM (black triangle) and P(3HS-*g*-3HT):PCBM (green triangle).

Not surprisingly, the initial carrier density of the gradient copolymer device is two orders of magnitude higher than the block copolymer. Furthermore, the gradient copolymer device showed the highest initial carrier density among all the devices consistent with the active layer of the gradient copolymer:PCBM having a much more continuous and interconnected fibril network, such as that shown in Figure 3.7. With the

highest initial carrier density, one might ask why then does the gradient copolymer device not out-perform the P3HT:PCBM "champion"? The answer lies in the free carrier recombination rates, which were extracted from the α exponent. The values are as follows: P3HT:PCBM, α = -0.80 ± 0.04 , P3HS:PCBM, α = -2.10 ± 0.01, P(3HS-*b*-3HT):PCBM, α = -1.45 ± 0.03 , and P(3HS-*g*-3HT):PCBM, α = -2.25 ± 0.03. This suggests that carrier recombination is most prevalent in the gradient copolymer device but for this device to maintain a decent performance, suggests that the large initial carrier generation compensates immensely for the numerous free carrier losses. In polymer:fullerene devices, recombination studies performed near open-circuit conditions have shown that V_{OC} and *FF* are limited primarily by nongeminate recombination.[104-107] The fact that even with higher recombination rates in the optimum gradient copolymer device its V_{OC} (0.6 V) and that of the P3HT device (0.6 V) are identical is suggestive of the existence of trap-assisted recombination in the gradient copolymer device.[104] Considering that the energetic landscape is influenced by variations in local ordering of the polymer structure driven by variations in conjugation length and also the magnitude of intermolecular interactions between polymer and fullerene,[108,109] it is likely that the differences in molecular arrangement and interaction between the 3HT, 3HS and fullerene components for each of the systems studied vary and this would influence the interplay between nanoscale morphology and electronic structure which ultimately affects the density of trap sites or recombination centers. One way to rationalize this is that the gradient copolymer device provides a decent trade-off between the high initial carrier density and recombination, by providing enough charge carriers to fill these trap

states while leaving an adequate amount available for transport and extraction at the respective electrodes.

3.2.6 Local Photocurrent Mapping

Having studied the optical properties, nanoscale morphology, crystallinity and carrier dynamics of our films and devices, it is now instructive to examine the local photocurrent generation using photoconductive atomic force microscopy (pcAFM). The samples were excited using a 532 nm diffraction limited laser and measurements performed at 0 V bias. These measurements were done on the same samples that were used for the bulk J-V measurements and scans were taken in areas between the top electrodes. Figure 3.9 shows the photocurrent maps of all the samples. This gives us an insight into why the P(3HS-*b*-3HT):PCBM performed poorly. We clearly see larger regions exhibiting low to no photoconductivity at all compared to all the other samples. We hypothesize that these regions are block copolymer-rich domains that have self-assembled and in the process excluded PCBM molecules, resulting in a decrease in the D/A interfacial area which leads to a decrease in photocurrent collection, low J_{SC} and PCE. This further corroborates the dense clusters of fibrils observed in the EFTEM images, which we concluded where the phase separated block copolymer-rich phase. Also, some of these regions could potentially be aggregates of PCBM. It would then seem that the inherent self-assembly property of rod-rod block copolymers is detrimental to device performance as is. On the other hand, the gradient copolymer device forms an interconnected structure between the polymer and fullerene leading to higher initial carrier density and improved performance over the block copolymer. Furthermore, our pcAFM study showed that not surprisingly, the P3HT:PCBM sample produced the

highest photocurrent. A qualitative examination of the 1:1 blend pcAFM image reveals large regions of relatively high photoconductivity similar to P3HT:PCBM, and regions of lower photoconductivity similar to P3HS:PCBM supporting our conclusion of their phase-separated domains.

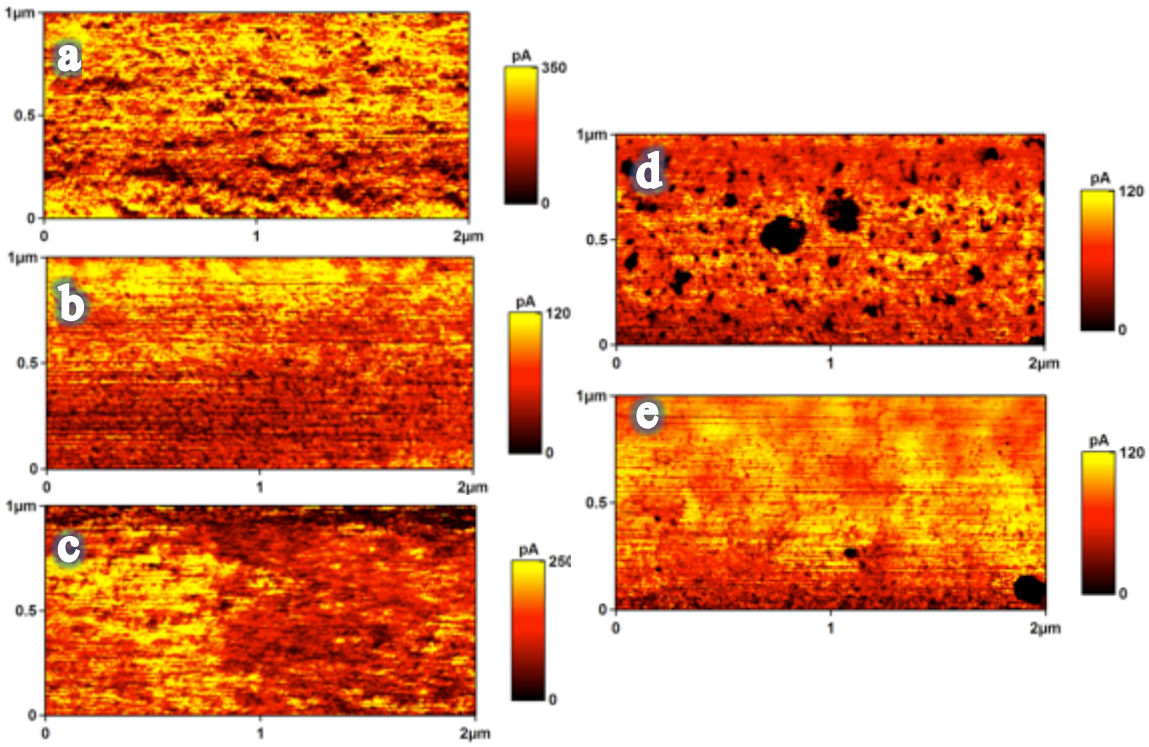

Figure 3.9 Photocurrent images from photoconductive AFM of (a) P3HT:PCBM (b) P3HS:PCBM (c) P3HS:P3HT:(1:1)PCBM), and (d) P(3HS-*b*-3HT):PCBM and (e) P(3HS-*g*-3HT):PCBM.

3.3 Relevance of Morphology to Device Performance

It is well established that phase separation in polymer:fullerene systems is driven by the crystallization behavior of the polymer.[43,110] In earlier work we showed that the morphologies and extent of phase separation of thin films of neat P(3HS-*b*-3HT) and P(3HS-*g*-3HT) vary significantly after isothermal recrystallization.[82] As discussed

earlier, we attribute the morphological differences observed, to the crystallization behavior of the copolymers, which is driven by the spatial arrangements of the 3HS block/segment along the copolymer chain. Therefore, the BHJ morphology, which influences device performance exhibited in the performance indicators, such as J_{SC}, V_{OC}, *FF* and *PCE*, is guided by the three-dimensional organization of the semicrystalline polymer during the active layer formation and/or subsequent processing procedure. Similarly, for the copolymer devices studied herein, the difference in comonomer sequence distribution along the backbone influences the variation in copolymer crystallization resulting in varying degrees of structural order as shown in our EFTEM and GIXD studies which manifest as differences in device performance. Our results indicate that phase separation in the block copolymer device, driven by the crystallization of the block copolymer, has an adverse effect on device performance, which could be caused by the dense clusters of pure-copolymer domains and an unfavorable morphology. On the other hand, the crystallization behavior of gradient copolymer provides a better nanoscale morphological structure that favors exciton dissociation in the gradient copolymer device.

3.4 Conclusion

We synthesized an all-conjugated copolymer of 3-hexylselenophene (3HS) and 3-hexylthiophene (3HT) in block and gradient sequence architectures and investigated their structure-performance relationships as donor materials in organic photovoltaic devices. We found that the comonomer ordering along the copolymer chain influences the optoelectronic properties, nanoscale morphology and device performance in the copolymer:fullerene system. Our EFTEM results show that the block copolymer had a

tendency to strongly self-assemble into dense clusters of pure-copolymer rich regions reducing its interfacial area with PCBM. Conversely, the gradient sequence shows an improved control of this innate self-assembly characteristic of copolymers while promoting interfacial activity between the copolymer and fullerene leading to a more continuous and interconnected fibril network with PCBM relative to the block copolymer and as a result generated the highest initial carrier density. All P3HS-containing devices where thermally stable relative to the P3HT-only device and this result was attributed to the higher degree of mixing of PCBM in the P3HS disordered polymer regions thereby suppressing PCBM aggregate growth with annealing.

Copolymer syntheses offer an opportunity through covalently linking comonomers in varying sequences, to merge the valuable properties of homopolymers yielding new and innovative materials. The all-conjugated copolymer approach via molecular design of 3HT and 3HS affords the ability to combine and optimize device efficiency (of P3HT) together with thermal stability (of P3HS) while tailoring BHJ nanoscale morphology. Owing to the rigid backbone and strong rod-rod interactions, fully π-conjugated copolymers behave distinctly different from other classes of copolymers, e.g., rod-coil copolymers. Block copolymers have long served as the material of choice to control nanoscale domain sizes and morphology for organic electronics applications,[111] however, our findings suggest that gradient copolymers could present new opportunities for tailoring the morphology and properties of an all-conjugated copolymer system.

In our study, we have shown that for π-conjugated copolymers that self-assemble and undergo intrinsic phase separation, a gradient sequence along the copolymer

backbone could be a potential approach to control and obtain a favorable nanoscale morphology required for optimum performance in photovoltaic systems and possibly other applications, and furthermore combine optoelectronic, physicochemical and thermal properties into one material.

3.5 Experimental Section

Polymer Synthesis: The copolymers were synthesized and characterized, as recently reported[82] (see **Error! Reference source not found.**). P3HS and P3HT were synthesized following reported procedures.[94,112] Polymer molecular weights were determined using gel-permeation chromatography (GPC) by comparison with polystyrene standards on a Waters 1515 HPLC instrument equipped with Waters Styragel® (7.8 x 300 mm) THF HR 0.5, THF HR 1, and THF HR 4 type columns in sequence and analyzed with Waters 2487 dual absorbance detector (254 nm). For P3HT, it was found that M_n = 31.2 kDa, $Đ$ = 1.18, regioregularity = 97%; for P3HS, M_n = 23.4 kDa, $Đ$ = 1.21, regioregularity = 98%; for P(3HS-*b*-3HT) M_n = 26.2 kDa, $Đ$ = 1.14, regioregularity = 97% and for P(3HS-*g*-3HT) M_n = 32.6 kDa, $Đ$ = 1.18 and regioregularity = 97%.^{1}H NMR and GPC spectra can be found in the Supporting Information.

Device Fabrication: Indium tin oxide (ITO)-coated aluminosilicate glass slides (Delta Technologies, Ltd.) were cleaned by ultrasonication sequentially in acetone and isopropanol for 20 min. A 4wt% Polyethylenimine, 80% ethoxylated (PEIE) and 2-methoxyethanol (Sigma Aldrich) solution was spin-coated in ambient atmosphere onto the ITO surface at 5000 rpm for 60s, then baked for 10 minutes at 100˚C to form an

approximately 10 nm PEIE film. The ITO/PEIE substrates were then transferred into an N_2-filled glovebox for device fabrication.

Devices were fabricated in an inverted architecture with the ITO/PEIE as the cathode. P3HT:PCBM (60:40), P3HS:PCBM (50:50), P(3HS-*b*-3HT):PCBM (55:45), P(3HS-*g*-3HT):PCBM (55:45) were dissolved in 1,2-dichlorobenzene (*o*-DCB) and stirred in the glovebox overnight at 80˚C. The solution was then filtered and the active layer spin-coated at 700 rpm for 30 s and thermally annealed at 150˚C for varying times in the glovebox. All P3HS-based samples were spin-coated on preheated substrates at 80˚C. Active layer thicknesses for all samples were in the range of 120 -140 nm as measured by spectroscopic ellipsometry (M 2000, J.A. Woollam Co.). To complete the device, the anode consisted of 15 nm MoO_3 and 100 nm Ag deposited through a 1mm diameter shadow mask by vacuum thermal evaporation (Angstrom Engineering PVD system). Devices were then tested in ambient under 1 sun illumination (100 mW cm^{-2}, AM 1.5) using an Oriel solar simulator, and the J-V characteristics were acquired using an Agilent 4156C Semiconductor Parameter Analyzer.

UV-Visible Spectroscopy: UV-vis absorption was measured using a PerkinElmer Lambda 750 Spectrophotometer.

External Quantum Efficiency (EQE): EQE measurements were performed on devices fabricated in the same manner as described above using collimated light from a halogen lamp coupled to a Newport 1/8m monochromator with a 5 nm FWHM output. The beam was optically chopped at 185 Hz and the photocurrent signal was detected using a Stanford Research Systems SR530 lock-in amplifier and compared to the output from a calibrated Si reference cell.

photo-CELIV: Devices were loaded in a cryostat (Janis VPF-100, vacuum pressure 1 mTorr) and exposed to laser pulses (Quantel BrilliantEazy, λ = 532 nm, pulse intensity ca. 20 μJ cm^{-2}). A function generator (BK Precision 4075) applied a linearly increasing voltage to extract the photo-generated current transient, which was passed through a preamplifier (FEMTO DLPCA-200) and recorded by a digital oscilloscope (Tektronix TDS3052C).

EFTEM: Measurements was performed on a JEOL 2100F TEM, using a slit width of 8 eV and an accelerating voltage of 200 kV. The active layer was spin-coated on a layer of PEDOT:PSS with the same casting and annealing procedures as described in the device fabrication procedure. The films were then sectioned using a razor blade and floated by immersion in deionized water onto copper grids with a supporting mesh (Ted Pella, Inc.).

GIXD: Grazing-incidence x-ray diffraction (GIXD) experiments were run on the G1 line (10.5 +/- 0.1 keV) at the Cornell High Energy Synchrotron Source. The beam was 0.05 mm tall and 1 mm wide. The x-ray beam was aligned such that it is above the critical angle of the polymer:fullerene film but below the critical angle of the substrate. Scattered intensity was collected with a two-dimensional Dectris® Pilatus detector, positioned 86.3 mm from the center of the sample. All images have been background subtracted.

pcAFM: All photoconductive atomic force microscopy (pcAFM) measurements were performed using an Asylum Research MFP-3D stand-alone AFM under ultrapure Ar purge (Cryogenic gases) in a closed fluid cell. A Pt/Ir5-coated contact-mode AFM probe (Nanosensors, ATEC-CONTPt, spring constant 0.2 N/m) was used as the top

contact allowing simultaneous determination of both topography and photocurrent recorded using the AFM's transimpedance amplifier. The source of illumination was a 532 nm diffraction limited laser focused and aligned to the probe, using a bottom-mounted objective. The illumination intensity was on the order of 10^4 W/m^2 for all devices.

3.6 Supporting Information

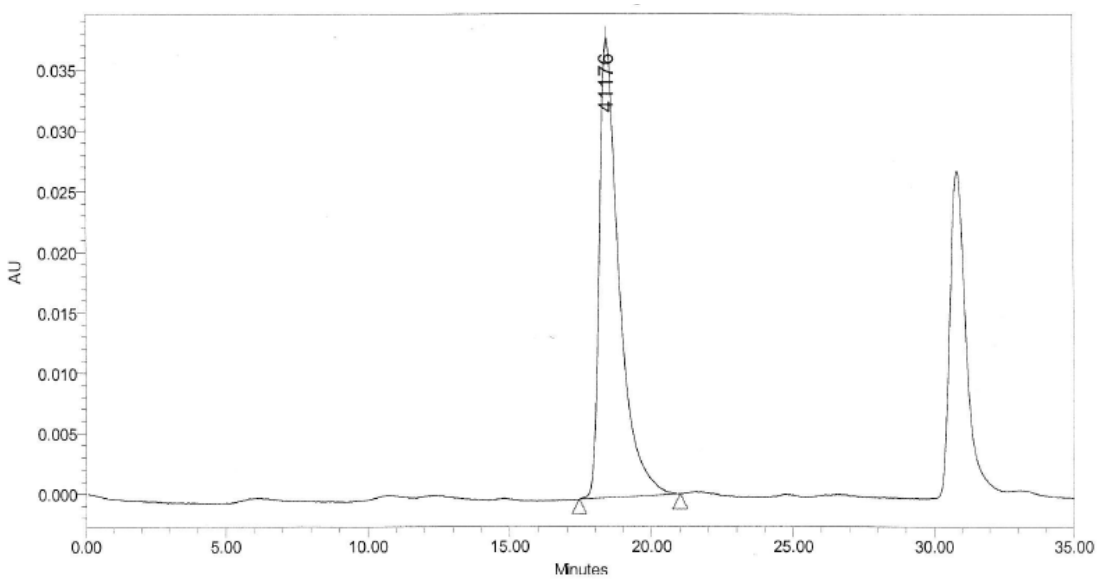

Figure 3.10 GPC of P(3HS-*g*-3HT)

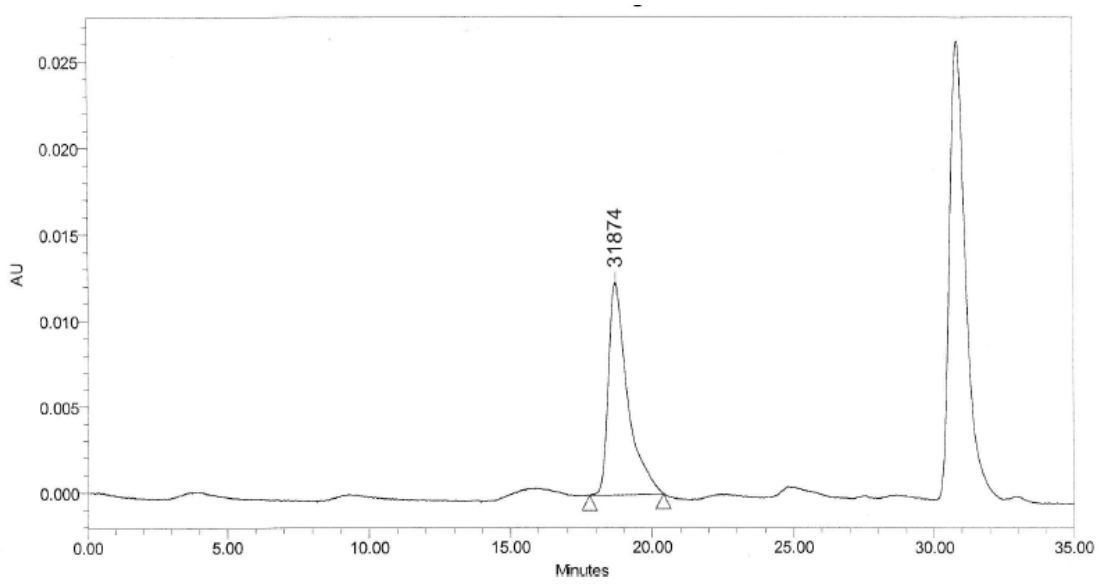

Figure 3.11 GPC of P(3HS-*b*-3HT)

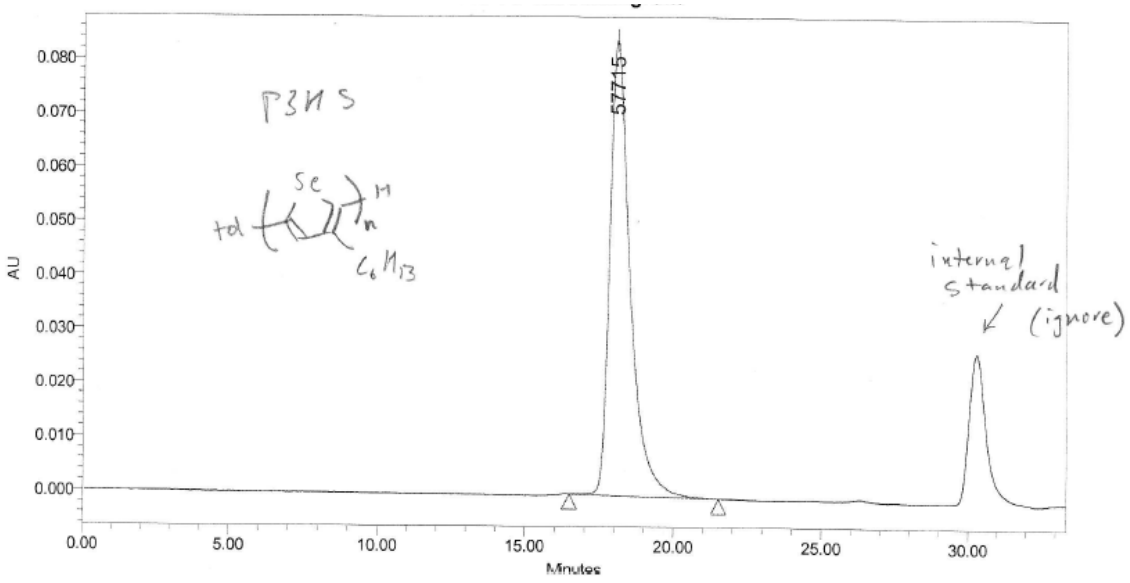

Figure 3.12 GPC of P3HS

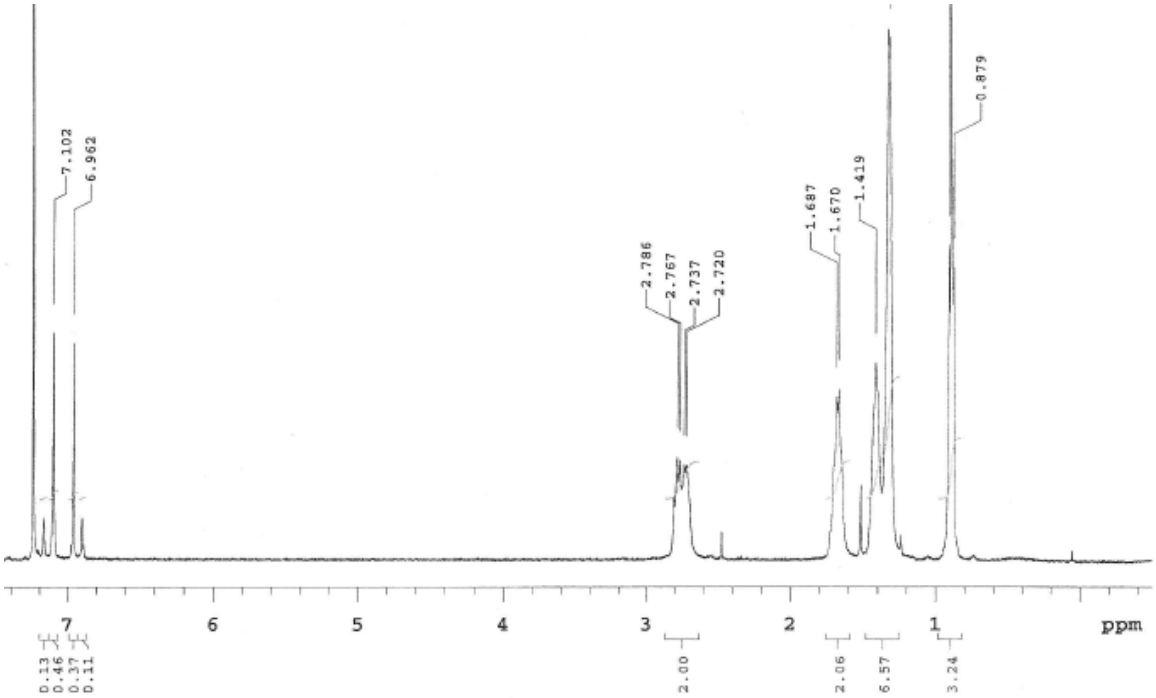

Figure 3.13 [1]H NMR spectrum of P(3HS-*g*-3HT)

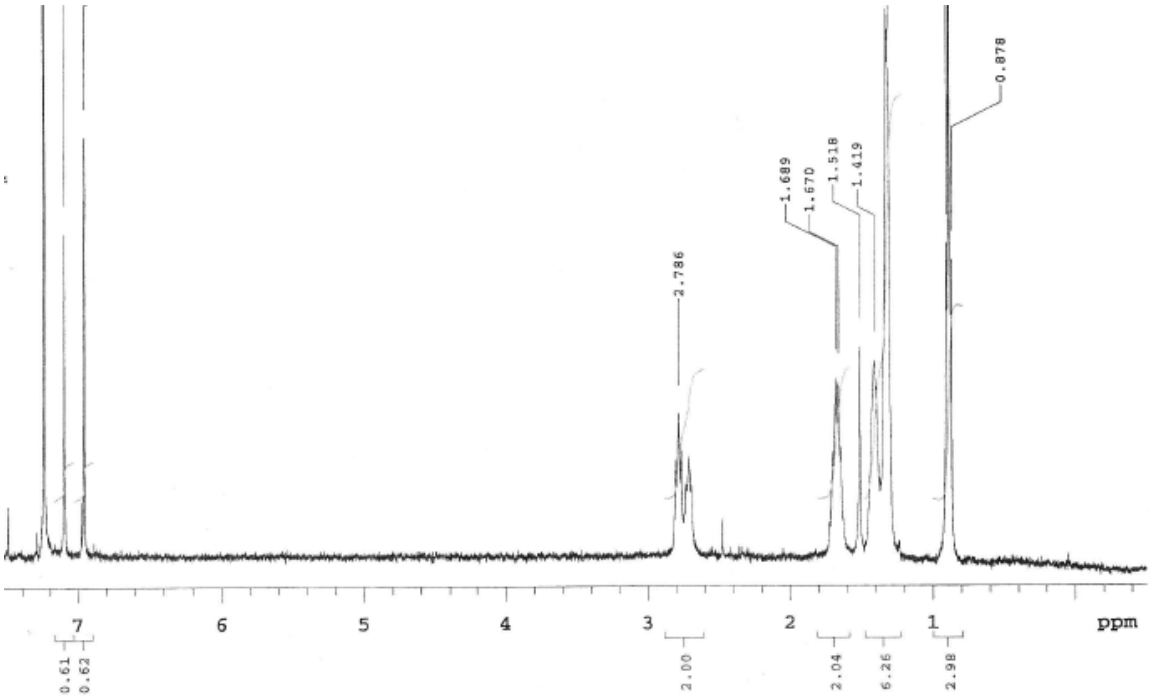

Figure 3.14 [1]H NMR spectrum of P(3HS-*b*-3HT)

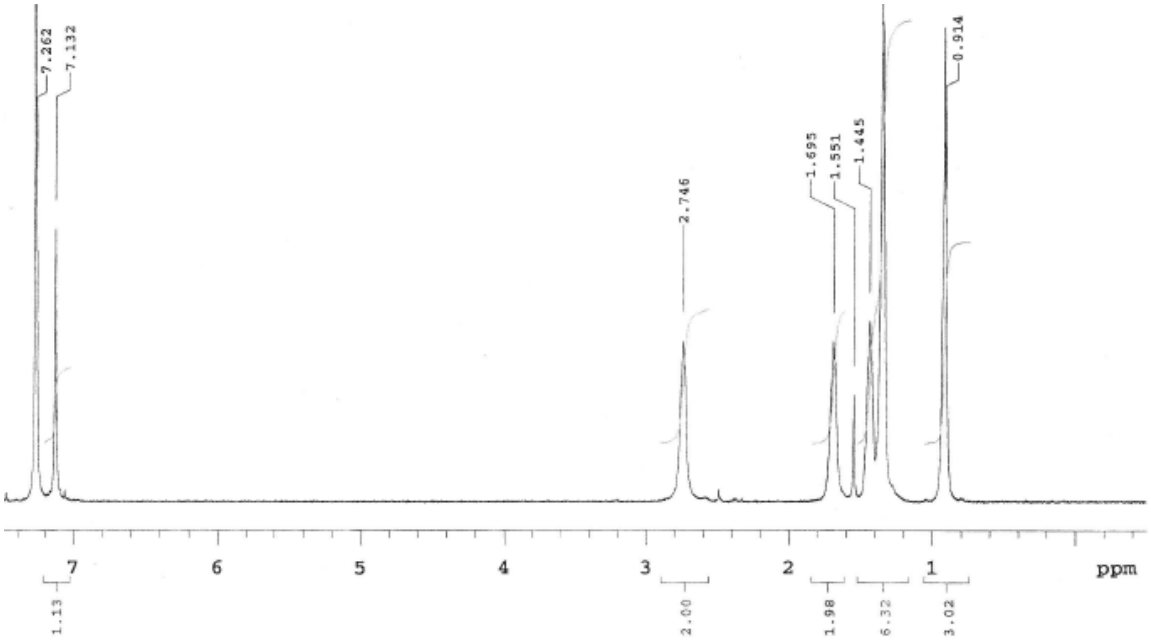

Figure 3.15 ^{1}H NMR spectrum of P3HS

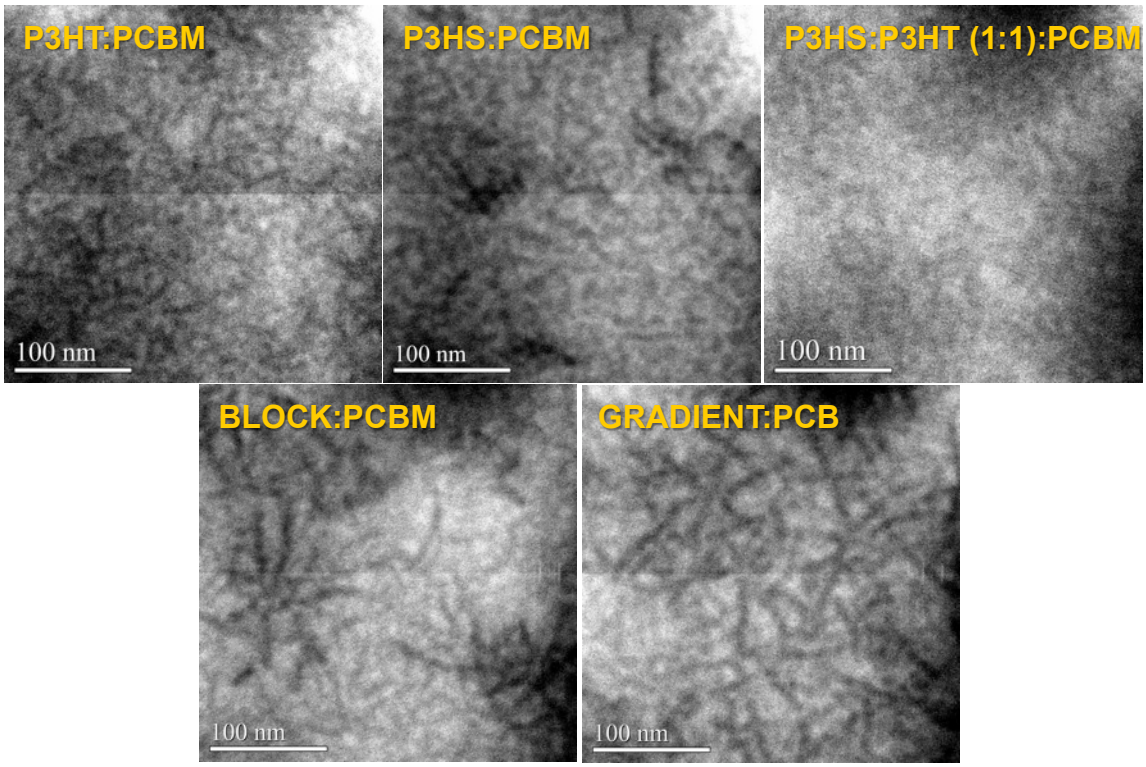

Figure 3.16 Higher magnification EFTEM images

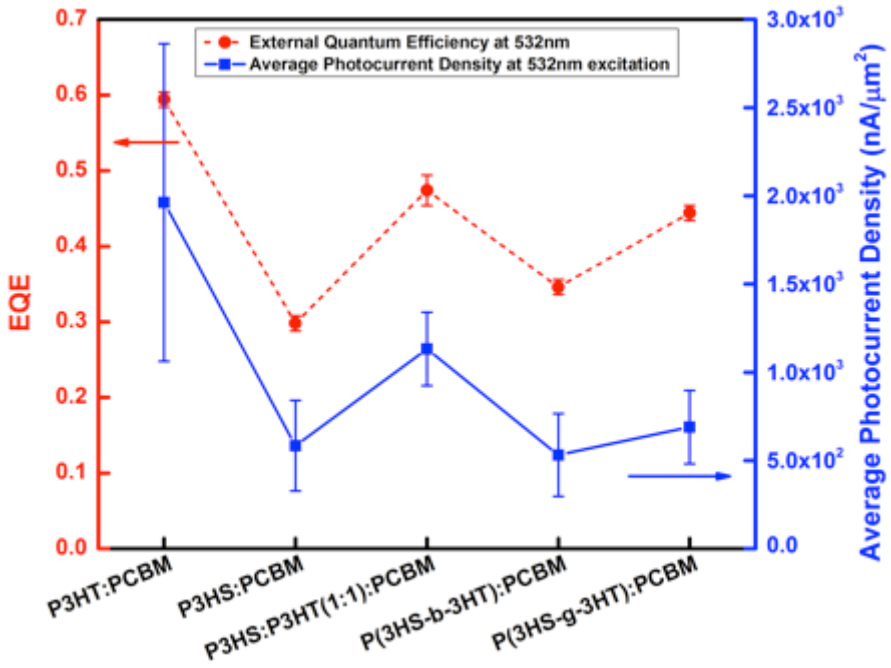

Figure 3.17 External quantum efficiency (EQE) at 532 nm monochromatic illumination is plotted on the left axis for each optimum device. Average photocurrent density from photoconductive AFM measurements is plotted on right.

CHAPTER 4:

Proof of Concept: Studying Interface-Directed Phase Separation in Thin Dielectric Films with Kelvin Probe Force Microscopy

In this section the concept of investigating the interfacial effects of thin polymer blend films using an established atomic force microscopy-based technique is introduced. This topic was pursued due to the authors' vast experience in AFM measurements.

4.1 Introduction

Kelvin probe force microscopy (KPFM) is a powerful technique that combines the versatility of atomic force microscopy (AFM), with the macroscopic Kelvin probe measurement, to detect local electrostatic forces and enable nanoscale mapping of the work function or surface potential, with high spatial resolution. In this context, the surface potential refers to the potential difference between the sample and a conducting probe in close proximity to the sample surface. Therefore, data obtained from KPFM measurements relates to the contact potential difference (CPD) between the sample surface and a conductive AFM probe. The short-range forces between the probe and sample can also affect the resolution of the CPD, which is between 5 – 20 mV. Since the establishment of KPFM by Nonnenmacher et al in 1991,[113] it has been increasingly

utilized to investigate the nanoscale electronic/electrical properties and interfacial phenomena of metals, organic and inorganic semiconductor materials and devices and biological materials.[114-118] In this thesis work, we have proposed to utilize KPFM to determine the vertical (out-of-plane) spatial organization and concentration profile of a heterogeneous polymer blend of poly(tetramethyl bisphenol polycarbonate) (TMPC) and polystyrene (PS). This system is an ideal case to study using this technique because it has been shown that TMPC and PS form a partially miscible blend below a lower critical solution temperature (LCST).[119,120] Such that, when thin TMPC/PS films on SiOx/Si substrates are annealed above the LCST, they exhibit a surface-directed spinodal decomposition phenomenon. The PS component tends to form a wetting layer and preferentially enriches the free surface due to its lower surface energy. On the other hand, TMPC has stronger interactions (hydrogen bonding) with the native silicon oxide substrate, forming an enriched polymer-substrate interfacial region.[120,121] The idea then is to use KPFM as a non-destructive and non-invasive tool to characterize the spatial organization of blend components in thin films and possibly distinguish between different chemical signatures, which demonstrate interfacial compositions that differ from the bulk. In this role, KPFM will serve to complement dynamic secondary ion mass spectroscopy (DSIMS), an established technique used to determine elemental composition and depth profiling of thin films. One advantage KPFM might have over DSIMS in depth profiling could be for use in functional devices and applications where sample destruction is not an option.

A prior study of surface potential measurements of molecular systems revealed that in these systems CPD is governed by dipole moments, which are dictated by

structural arrangements, packing densities, molecular orientations and chemical structure.[122] Recently, an experimental and simulation study of KPFM on dielectrics concluded that the measurements are sensitive to both the surface and sub-surface regions, and also the electric field of the tip penetrates into the sample such that contributions from the substrate can be detected.[123] This is one of reasons why we chose to pursue this research route in using KPFM to study the interface-directed phase separation in TMPC/PS thin films, since based on their chemical structures alone (see Figure 4.1), we would expect the two homopolymers to exhibit a difference in surface potential.

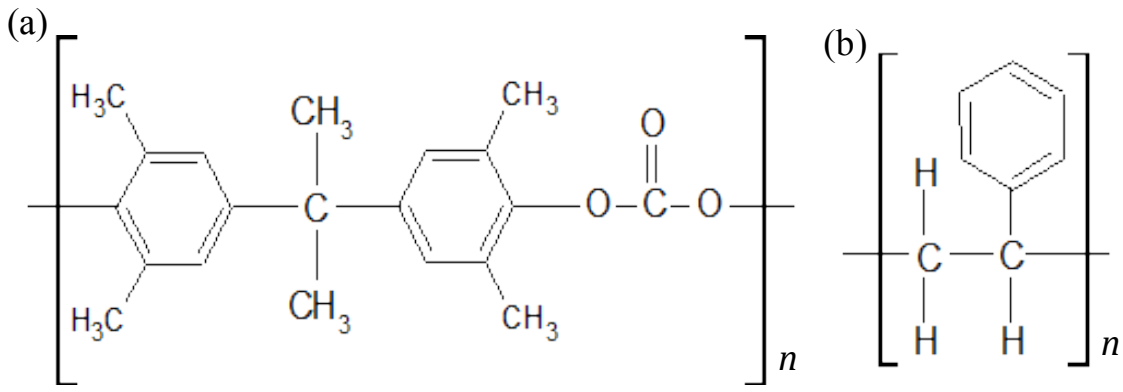

Figure 4.1 Chemical structures of (a) TMPC and (b) PS

4.2 Operating Principle of KPFM

KPFM is the nanoscale variant of the classical Kelvin probe method originally developed by Lord Kelvin in 1898.[124] In this early experiment, Lord Kelvin showed that one could resolve the contact potential difference between two circular metallic plates, made of Cu and Zn, by creating a parallel plate capacitor between the plates. By generating a periodic change in the separation distance of the plates, a change in

capacitance resulted in an alternating current (AC) in an external circuit connecting the plates. Furthermore, irrespective of the medium between the plates, applying a DC bias corresponding to the CPD between the plates could annul this AC. Consequently, if one of the plates has a known work function; it could then be used as a reference to determine the surface potential or work function of the other plate.

KPFM operates on the same basic principle, however, rather than detecting the AC generated, the electrostatic force between a conductive AFM probe and the sample is used to determine the CPD. This is primarily because in an AFM and on the nanoscale, it is relatively easier to detect and measure force rather than current, which are typically on the order of a few pico Amps or hundreds of femto Amps. In addition, instead of providing an average of the CPD over the sample surface, KPFM provides a nanoscale map of the CPD distribution of a sample simultaneously with the topography. Although the operating principle appears straightforward, the consistency and quantitative analysis of KPFM data requires very careful assessment of the influence of environmental conditions and various experimental parameters.[114]

There are two basic approaches to performing KPFM. These are, (a) Lift mode and (b) Dual-frequency mode.[125] In this thesis the lift mode approach is used and its details are discussed below. As shown in Figure 4.2, the lift mode technique uses a double pass method; therefore for each line in an image, two scans are performed. On the first pass (1) the tip maps the topography where the amplitude of the mechanical oscillation, driven at the first resonance frequency of the cantilever, is used as the feedback signal to obtain surface topography.

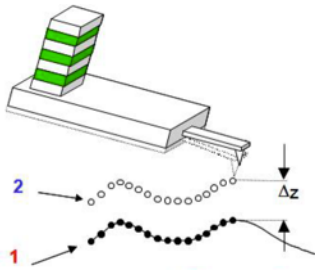

Figure 4.2 A schematic of KPFM double pass scanning mode.

On the second pass (2) the mechanical oscillations of the tip is set to zero while it is lifted along the z direction a known distance above the sample surface. This distance, known as the lift height (Δz), is typically 10 - 20 nm, outside the range of Van der Waal forces. To minimize the cross-talk between the topography and CPD signals, the motion of the tip in the second pass follows the same route from the first pass in a closed loop feedback. Furthermore, on the second pass, an AC bias is sent to the AFM tip at its resonance frequency which generates an electric force on the cantilever. At this juncture, the interaction between the tip and sample can be modeled as a parallel plate capacitor, with the force proportional to the square of the total bias between the tip and sample, as in equation (4.1). This total bias is a summation of the samples' potential difference plus any DC and AC bias applied see equation (4.2).

$$F(z) = -\frac{1}{2}\frac{\partial C}{\partial z}\Delta V^2 \tag{4.1}$$

$$\Delta V = V_{sample} + V_{DC} + V_{AC}\sin(\omega t) \tag{4.2}$$

Substituting equation (4.2) into (4.1) and solving for F, we obtain a static component (independent of ω), equation (4.3), an ω component, equation (4.4) and a 2ω component, equation (4.5) of the force.

$$F_{static} = -\frac{1}{2}\frac{\partial C(z)}{\partial z}\left[\left(V_{DC} + V_{sample}\right)^2 + \frac{1}{2}V_{AC}^2\right] \tag{4.3}$$

$$F_{\omega} = -\frac{\partial C(z)}{\partial z}\left[\left(V_{DC} + V_{sample}\right)V_{AC}\sin(\omega t)\right] \tag{4.4}$$

$$F_{2\omega} = \frac{1}{4}\frac{\partial C(z)}{\partial z}\left[V_{AC}^2\cos(2\omega t)\right] \tag{4.5}$$

Additionally, during the second pass, a lock-in amplifier is employed to measure the ω component of the force, F_{ω}, equation (4.4), after which the potential feedback loop is then used to adjust V_{DC} to the tip to nullify F_{ω} (F_{ω} = 0). In this instance, $V_{DC} = V_{CPD}$, the contact potential difference between the tip and sample surface. The 2ω component, $F_{2\omega}$, can be used for nanoscale dielectric spectroscopy and capacitance microscopy measurements,[125] which is beyond the scope of this thesis. Since KPFM is a relative measurement, the work function of the tip has to be calibrated before each sample is scanned in order to obtain an absolute surface potential value. The calibration sample generally used is highly ordered pyrolytic graphite (HOPG), with known work function (ϕ_{HOPG} = 4.6 eV). The sample's work function or surface potential is then calculated using equation (4.6), where ϕ_{tip} and ϕ_{sample} are the work functions of the tip and sample respectively, and e is the electron charge. In KFPM measurements, it is important to find the minimum lift height or the closest tip-sample distance, which is just outside the range

of Van der Waal forces since the resolution and sensitivity of the CPD measurements decreases at large Δz distances. One drawback to lift mode however is that it is time consuming because of its two-step process to data acquisition, in addition to the fact that ideally much slower scan speeds must be used relative to just regular topography scans.

$$V_{DC} = V_{CPD} = \frac{\phi_{tip} - \phi_{sample}}{-e} \tag{4.6}$$

We will now briefly discuss the second approach (b). For the dual frequency mode, unlike lift mode, each line in an image represents only one scan. The tip is mechanically driven at the first resonance frequency, which is used as feedback for the topography signal. At the same time, a phase locked loop controls the second-order resonance; this second oscillation mode can be about six times larger than the fundamental resonance frequency, and it is used as feedback for the CPD.[126] By using two separate lock-in amplifiers the two signals are decoupled minimizing any cross-talk.[125]

4.2.1 Detecting F_ω: Amplitude Modulation and Frequency Modulation

As discussed earlier, one of the critical steps during the KPFM measurement is the effectiveness of the lock-in amplifier to detect and annul the electrostatic force F_ω. There are two methods commonly used to detect F_ω; Amplitude modulation (AM) and Frequency modulation (FM). In AM, the oscillation amplitude of the cantilever is the signal used by the lock-in amplifier to measure F_ω. Once F_ω is detected, a potential feedback loop is engaged and a range of DC voltages is applied at each point. The minimum voltage that nullifies F_ω is then recorded as the CPD.

Typically for any FM-based measurement; interaction between the tip and sample is detected by shifts in the oscillation frequency of the cantilever at constant amplitude. Therefore for FM-KPFM, a lock-in amplifier detects the frequency shift used to determine the force gradient dF_ω / dz. A DC voltage (V_{CPD}) is then applied to nullify this change in frequency. One notable advantage of AM-KPFM relative to FM-KPFM is, since the resonance condition of the amplitude is used, AM-KPFM shows a significant improvement in signal-to-noise ratio over FM-KPFM.[126] In this work AM-KPFM is utilized on an Asylum Research MFP-3D stand alone Atomic Force Microscope with a built-in lock-in amplifier operated in KPFM mode. Platinum Silicide (PtSi) probes with resonance frequency of 330 kHz and force constant of 42 N/m (PtSi-NCH, NanoSensors) were used for the KPFM experiments. The work functions of the probes were calibrated on reference substrates of freshly cleaved HOPG (ZYA Quality / Mosaic Spread 0.8°±0.2° / Grain size up to 10µm / Size1.5x10x10 mm, Ted Pella, Inc). All KPFM scans were done at room temperature under purge of ultra pure grade Ar gas.

4.3 Surface Potential Measurements of TMPC/PS Dielectric thin films

Since its inception, KPFM has become an essential tool for studying electronic properties at the nano- and meso-scales. Very recently, the notion of extending the capabilities of KPFM measurements to purely dielectric material systems on insulating substrates has been a subject of major interest which is being explored in both theory and experiments.[123,127-130] Despite the tremendous amount of work already done, the fundamental physics governing the electrostatic interaction between the conductive tip

and insulating sample together with the detailed interpretation of the CPD data for dielectric samples is still not yet fully understood. Nonetheless, we report herein results of our initial study of KPFM on miscible TMPC/PS polymer blends.

4.3.1 Experimental Details

The polymer blend thin films were prepared as follows: TMPC (Bayer, M_w = 38 kg/mol, PDI = 2.75) and PS (Pressure Chemical, M_w = 49 kg/mol, $Đ$ = 1.06) were dissolved in toluene separately and mixed in varying weight ratios, (TMPC:PS, 0:1, 0.25:0.75, 0.5:0.5, 0.75:0.25, and 1:0). The solutions where then spun onto silicon substrates (Wafer World) with approximately 1.8 nm native oxide layer to obtain film thicknesses of 900 nm as measured with spectroscopic ellipsometer (JA Woolam, M-2000). Each film was then annealed at a temperature 10°C above its Tg for 4 hours in a vacuum oven. The neat TMPC and neat PS were annealed at 230°C and 110°C respectively. The blend films were annealed as follows; 0.25:0.75 at 147°C, 0.5:0.5 at 170°C and 0.75:0.25 at 187°C. All KPFM measurements were performed in an inert environment of ultra pure Ar gas purge. To ensure reproducibility, multiple measurements were done for the same sample on different days using the same tip.

4.3.2 Results and Discussion

Topography and contact potential difference maps, representing the raw data from KPFM measurements, are shown in Figure 4.3.

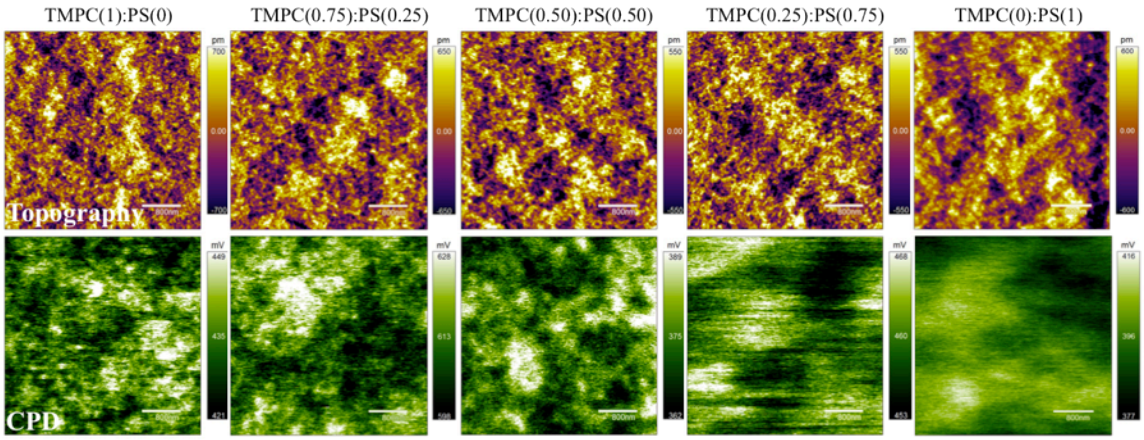

Figure 4.3 Topography (top row) and contact potential difference (bottom row) maps of (from L to R) neat TMPC, TMPC(0.75):PS(0.25), TMPC(0.5):PS(0.5), TMPC(0.25):PS(0.75) and neat PS thin films of thickness, $h \sim 900$ nm. The scale bar is 800 nm.

From a cursory look at the CPD images, we can qualitatively infer there is a correlation between CPD and blend ratio and also the CPD maps of neat TMPC and PS are markedly different in terms of resolution. The root-mean-square (RMS) roughness of all the samples is approximately 0.41 nm ± 0.03 and no differences can be deduced from the topographical features, especially for the neat TMPC and PS. For each sample a minimum of three scans were performed in order to obtain consistent results and standard deviation for the surface potential values shown in Figure 4.4 after taking into account the work function of the conductive probe.

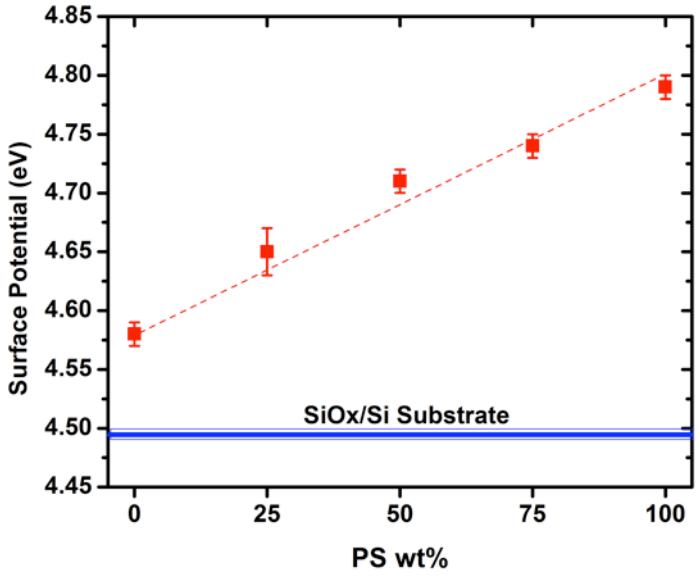

Figure 4.4 Surface potential values vs blend ratio of TMPC/PS thin films of thickness $h \sim$ 900 nm. The dashed red line serves as a guide to the eye. The blue line represents the surface potential, including its standard deviation, of a freshly cleaned bare SiOx/Si substrate measured under the same conditions as the samples.

We observe from the data in Figure 4.4 that the surface potential increases monotonically with PS wt% from neat TMPC (0 PS wt%) to 100 PS wt%. This suggests that the KPFM measurement is sensitive to the blend composition such that, as PS wt% increases the surface potential begins to approach that of the neat PS. In the TMPC/PS blend, as mentioned above, the substrate is enriched with TMPC, due to highly specific interactions (hydrogen bonding) between the C=O segments on TMPC and hydroxyl (OH) groups at the SiOx interface, on a length scale of few monomers, and the free surface is PS-rich due to lower surface energy. It has been shown that the structure of the bulk depicts that of a heterogeneous miscible blend, and due to self-concentration effects is represented by TMPC-rich and PS-rich regions at nm length scales.[120] Since the surface potential values of the blends seem to represent the weighted average of the neat cases, we hypothesize that the surface potential exhibits those of the distinctive TMPC and PS

components. Furthermore, this shows that the measurement probes an average blend composition of the bulk, which would then imply that there is a length scale or probing depth associated with KPFM. Specific experiments to discern this sampling depth are currently being pursued by my successor and would be reported later.

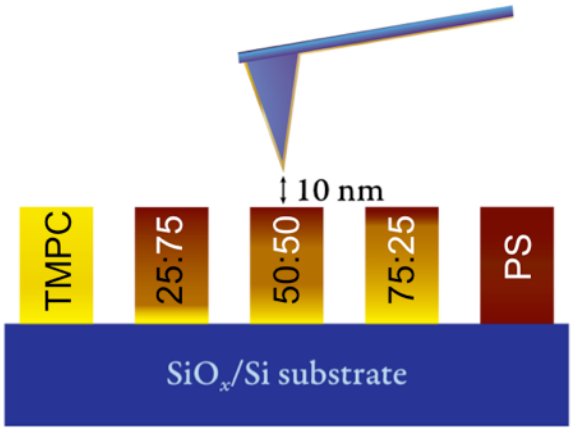

Figure 4.5 Schematic of KPFM measurement showing thin films with color-coded distribution of TMPC and PS components for the blends and neat cases on SiOx/Si substrate.

4.4 Conclusion

We have shown that for a miscible blend that shows an interface-directed phase separation behavior, KPFM is a promising tool to investigate the vertical spatial organization of individual components. Furthermore, our initial results show that the surface potential values are close to a weighted average of the neat cases indicative of sampling over an effective volume associated with a depth of probe from the surface. This also shows that for dielectrics, referring to the data from KPFM as surface potential might be perhaps a misnomer since the electric field penetrates into the sample and probes the bulk or sub-surface volume.

Interpreting the data obtained from KPFM on insulating materials still remains a challenge. The fact that the bulk volume is probed during the measurement needs to be further elucidated prior to applying this non-invasive technique to a wider range of applications. In addition, regarding the probe depth, an important question that needs to be addressed would be, is this length scale material dependent? Once these and other questions are resolved, utilizing KPFM for studying interface dependent phase separation in thin films will open new doors for exploration of more complex polymeric systems.

CHAPTER 5:

Conclusions and Future Work

In this work, we have demonstrated approaches to tailoring the morphology of polymeric organic photovoltaics in chapters 2 and 3. We have also shown in chapter 4 that we can utilize KPFM to probe the depth profile of polymer blend thin films and study interfacial effects. In chapter 2 we proposed supercritical carbon dioxide ($scCO_2$) as an alternative strategy to promote optimal phase separation, and purity, between the donor and acceptor of polymer bulk heterojunction solar cells. By controlling the pressure, temperature and density of $scCO_2$, our results revealed that the performance of a P3HT/$PC_{61}BM$ solar cell, J_{SC}s and PCEs, was comparable to and in some cases better than devices processed using the conventional high temperature thermal annealing procedure. Furthermore, by using photoconductive AFM we showed that a larger fraction of regions that exhibit photoconductivity was associated with improved device efficiency and the lowest active device areas, and most phase mixed regions, were exhibited by the as-cast samples. The results reported in chapter 2 reveal that $scCO_2$ is a mildly plasticizing solvent, which has a preferential affinity for the polymer component and furthermore promotes nanoscale phase separation, necessary to improve device efficiency

compared to the higher temperature thermal annealing where active components start to degrade after a rather short time.

In chapter 3 we demonstrated that for π-conjugated copolymers that self-assemble and undergo intrinsic phase separation, a gradient sequence along the copolymer backbone could be a potential approach to control and obtain a favorable nanoscale morphology required for optimum performance in polymer photovoltaic systems. Compared to the block copolymer, which had a tendency to strongly self-assemble reducing its interfacial area with PCBM, the gradient sequence showed an improved control of this innate self-assembly characteristic of copolymers while promoting interfacial activity between the copolymer and fullerene leading to a more continuous and interconnected fibril network with PCBM relative to the block copolymer and as a result generated the highest initial carrier density. Furthermore, all P3HS-containing devices where thermally stable relative to the P3HT-only device and this was attributed to the higher degree of mixing of P3HS disordered polymer regions with PCBM suppressing PCBM aggregate growth with annealing.

In Chapter 4 we introduced a proof of concept and showed that for a miscible blend that shows an interface-directed phase separation behavior, KPFM is a promising tool to investigate the vertical spatial organization of individual components. Furthermore, our initial results show that the surface potential values are close to a weighted average of the neat cases indicative of sampling over an effective volume associated with a depth of probe from the surface.

This thesis work has focused on novel methods to control the morphology of polymer-based photovoltaic devices as well as expanding on the capabilities of KPFM to

measure interface sensitive phase separation in polymer blends. Bulk heterojunction polymeric photovoltaic systems have an advantage of providing economically viable, lightweight, flexible and solution-based fabrication of thin film solar cell technology. In summary, the optoelectronic processes in OPV devices is dependent on the morphology and structural arrangement of the photoactive materials therefore the methods for morphological control introduced herein have contributed to knowledge in the field and hopefully hold promise for adoption by researchers, engineers and scientists.

5.1 Appendix

It is increasingly important to gain a deeper understanding of the optoelectronic processes at the nanoscale in order to continue exploring and developing novel high performance materials for organic electronic devices. The atomic force microscope (AFM) is an important tool for nanoscale electrical and morphology characterization throughout our work. In the following appendix/subsection, the basics of AFM imaging modes and a few techniques set up by the author for nanoscale electrical measurements used in this thesis are explained.

5.2 Atomic Force Microscopy

Binnig et al first introduced the AFM in 1986 as a technique to measure surface features below the optical diffraction limit.[131] Since then, the AFM has advanced to be one of the most versatile tools with nm scale resolution used to study surface morphologies and nanoscale phenomena, for example mechanical, magnetic, dielectric, electrical, ferroelectric and piezoelectric properties of various material systems such as polymers, biological membranes, inorganic semiconductors and metals. The basic components of an AFM are piezoelectric scanners, a force sensor and feedback controllers. AFMs operate by detecting the force between a sharp tip mounted at the apex of a cantilever and the sample surface and then raster-scanning over the surface. During this process, a feedback loop when engaged sends signal back from the force sensor to the piezoelectric scanner, which allows it to maintain either a constant force or constant height between the tip and the surface while data of interest (e.g. topography) is acquired

and mapped. The probes are typically made of silicon or silicon nitride (Si_3N_4) and can also be metallized for electrical measurements or to increase the reflectivity of the signal to the force sensor. The cantilever design can either be diving-board-shaped or V-shaped. The tip radius, which determines the lateral resolution, ranges from a few to several tens of nm.

The force senor is based on an optical lever detection system, where a laser beam is reflected from the backside of the cantilever onto a four-segment photodetector. The basic principle for detecting the force is based on Hooke's law, $F = -k\delta$, where k is the spring constant of the cantilever (ranges between 0.01 – 50 N/m) and δ is the deflection of the cantilever, that is, the distance the cantilever bends when it interacts with the surface. The cantilever can either bend vertically upwards or downwards towards the surface depending on the nature of the interaction, which may be repulsive or attractive (see Figure 5.1). Furthermore, the types of forces experienced by the tip have both short- and long-range contributions and are therefore are a function of tip-sample separation distance and also material properties of the sample. The forces, can be on the order of a few pN to tens of nN, and also vary based on the operating mode and conditions used for imaging as shown in Figure 5.1.

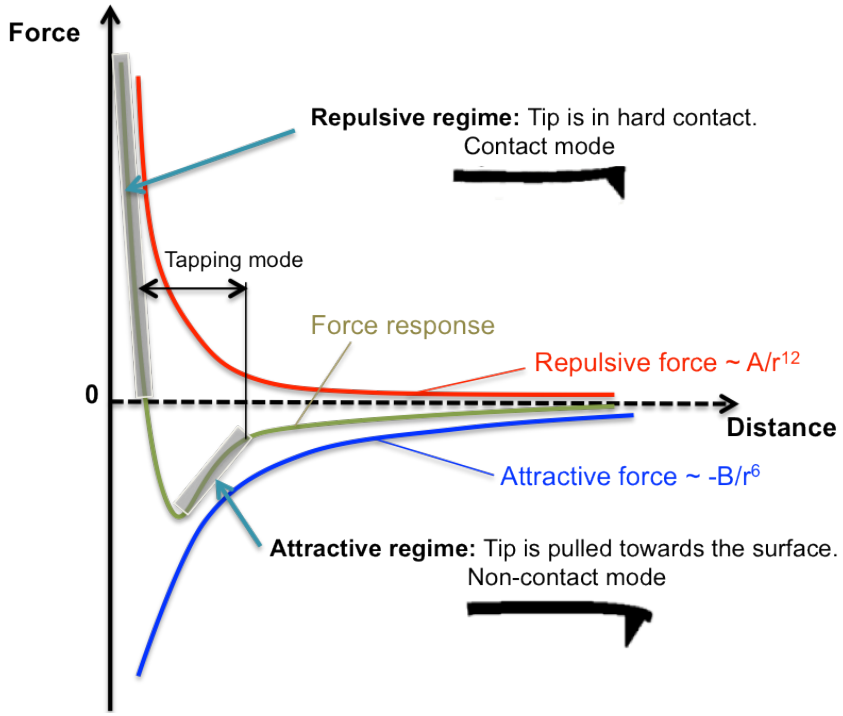

Figure 5.1 Force vs tip-sample separation distance showing operation regimes. The force response curve represents the tip-sample interaction, a superposition of the attractive and repulsive force curves.

5.2.1 AFM Operation Modes

As shown in Figure 5.1, the basic operation modes are *contact*, *tapping (intermittent contact)* and *non-contact* modes. Contact mode is the simplest mode and self-explanatory, in this mode, the tip is in hard physical contact with and always touching the surface in the repulsive regime. Typically most AFMs operate in constant force in contact mode. This means the feedback system works to keep the cantilever vertical deflection constant at a value (set-point) determined by the user. Therefore to optimize imaging, the set-point and feedback mechanism, fine-tuned through the integral gains, must be adjusted appropriately. The topography (height) data acquired is then the correction to the vertical deflection signal by the feedback control via height adjustment by the piezoelectric scanner to keep the deflection/force constant. For polymeric and

biological samples the spring constant of probes used for contact mode is typically on the lower end (0.01 – 2 N/m), to ensure minimal forces and prevent sample damage. Furthermore, for diving-board-shaped cantilevers, the lateral deflection can provide extra information to understand the frictional properties of the surface. In this work, contact mode is utilized for conductive and photoconductive AFM.

Both tapping and non-contact modes are classified as dynamic modes where the probe is mechanically oscillated either at or near its resonant frequency (70 – 400 kHz). The probes used for dynamic modes have higher spring constant (2 – 50 N/m) and stiffer than those for contact mode to avoid being pulled into hard contact with the surface. The basis of operation is that as the oscillating probe interacts with the sample, the oscillations are dampened which can be detected via changes in the amplitude, phase or frequency, a feedback loop is then engaged to maintain a constant probe–sample interaction as data is obtained. The main differences between the dynamic modes are in the magnitude of the amplitudes of the mechanical oscillation and the method used for detecting changes in oscillation. The amplitude of the mechanical oscillations determines the tip-sample forces and interaction, for non-contact mode, small amplitudes (~10 nm)[132] are used, which ensure the cantilever remains in the attractive regime only with small probe–sample forces (tens of pN). This minimizes tip wear and is beneficial for imaging very soft samples. On the other hand, the probe is oscillated with larger amplitudes (1 – 100 nm)[133] in tapping mode. This means the tip–sample interaction can be tuned to be in either the repulsive or attractive regimes. The repulsive regime offers much higher resolution however since the tip makes hard contact with the sample, there exist possibilities of tip wear and sample damage. The amplitude, frequency or phase

signals can be used for detecting changes in oscillation. Amplitude modulation (AM-AFM) is when the amplitude signal is used for feedback control and frequency modulation (FM-AFM) is when the frequency signal is controlled by the feedbacks. These can either be in tapping or non-contact modes. For the Kelvin probe force measurements (KPFM) presented here tapping mode AM-AFM was utilized. For more details of the KPFM set-up and operating principle the reader can refer to chapter 4.

5.2.2 Conductive and Photoconductive Atomic Force Microscopy

In recent years, conductive atomic force microscopy (cAFM) and photoconductive atomic force microscopy (pcAFM) have been employed to probe the local electrical and optoelectronic properties, respectively, with nanometer scale resolution in the field of organic electronics.[36,134,135] In cAFM, a conductive probe is brought into contact with the sample surface while a voltage is applied across the sample and current injected from either electrode dependent on the polarity of the applied bias, Figure 5.2. As the probe is raster-scanned over the sample, the dark current and topography data are simultaneously obtained, with pico to femto Ampere current sensitivity and nanometer resolution. CAFM is useful in domain size characterization of conductive polymers and small molecules blends with fullerenes, for photoactive layers, or insulating molecules for buffer layers.

PcAFM is a modification of cAFM whereby a diffraction-limited laser, which may be attenuated by neutral density filters, is aligned to the probe for photoexcitation of the sample region in close proximity of the probe location. This technique provides direct information about the local photoresponse of the composition-dependent optoelectronic properties of organic thin film solar cells. Both these measurements require precise nN

force control to prevent sample damage while still applying enough force to track topographical features. However, pcAFM still requires further development to expand the capabilities of the technique to study photo-degradation and obtain useful quantitative information that will complement degradation studies under 1 sun.

Also, due to the sensitivity of organic materials to oxygen and moisture, pcAFM and cAFM measurements are performed in an ultra pure Ar environment in a closed fluid cell. Furthermore, another precaution that should be considered when loading and unloading the conductive probes is to ground oneself especially during the winter months when static electricity is very prevalent, in order to preserve the conductive metallic coating on the probes.

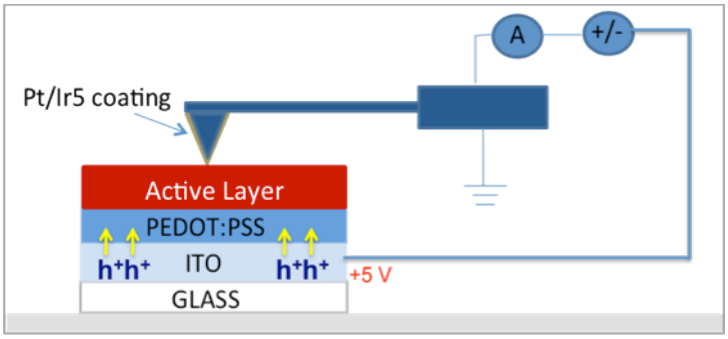

Figure 5.2 A schematic of cAFM set-up, with bias applied to the substrate

References

(1) Darling, S. B.; You, F. Q. *Rsc Adv* **2013**, *3*, 17633.

(2) B. Metz, O. R. D., P.R. Bosch, R. Dave, L.A. Meyer; IPCC, 2007: Climate Change 2007: Mitigation. Contribution of Working Group III to the Fourth Assessment Report of the Intergovernmental Panel on Climate Change: Cambridge University Press, 2007.

(3) International Energy Statistics Electricity Generation (most recent data available December 18 2014).

(4) World net electricity generation by fuel International Energy Outlook 2013 Chapter 5 Electricity Figure 83.

(5) Green, M. A.; Emery, K.; Hishikawa, Y.; Warta, W.; Dunlop, E. D. *Prog Photovoltaics* **2013**, *21*, 827.

(6) Shirakawa, H.; Louis, E. J.; Macdiarmid, A. G.; Chiang, C. K.; Heeger, A. J. *J Chem Soc Chem Comm* **1977**, 578.

(7) Heeger, A. J. *Angew Chem Int Edit* **2001**, *40*, 2591.

(8) Balint, R.; Cassidy, N. J.; Cartmell, S. H. *Acta Biomater* **2014**, *10*, 2341.

(9) Pope, M.; Swenberg, C. E.; Pope, M. *Electronic processes in organic crystals and polymers*; 2nd ed.; Oxford University Press: New York, 1999.

(10) Marsh, R. A.; Hodgkiss, J. M.; Albert-Seifried, S.; Friend, R. H. *Nano Lett* **2010**, *10*, 923.

(11) Tang, C. W. *Appl Phys Lett* **1986**, *48*, 183.

(12) Yu, G.; Gao, J.; Hummelen, J. C.; Wudl, F.; Heeger, A. J. *Science* **1995**, *270*, 1789.

(13) Yang, F.; Sun, K.; Forrest, S. R. *Adv Mater* **2007**, *19*, 4166.

(14) Li, G.; Shrotriya, V.; Huang, J. S.; Yao, Y.; Moriarty, T.; Emery, K.; Yang, Y. *Nat Mater* **2005**, *4*, 864.

(15) Zhao, Y.; Xie, Z. Y.; Qu, Y.; Geng, Y. H.; Wang, L. X. *Appl Phys Lett* **2007**, *90*.

(16) Moule, A. J.; Meerholz, K. *Adv Funct Mater* **2009**, *19*, 3028.

(17) Treat, N. D.; Brady, M. A.; Smith, G.; Toney, M. F.; Kramer, E. J.; Hawker, C. J.; Chabinyc, M. L. *Adv Energy Mater* **2011**, *1*, 82.

(18) Verploegen, E.; Mondal, R.; Bettinger, C. J.; Sok, S.; Toney, M. F.; Bao, Z. A. *Adv Funct Mater* **2010**, *20*, 3519.

(19) Gomez, E. D.; Barteau, K. P.; Wang, H.; Toney, M. F.; Loo, Y. L. *Chemical Communications* **2011**, *47*, 436.

(20) Wu, W. R.; Jeng, U. S.; Su, C. J.; Wei, K. H.; Su, M. S.; Chiu, M. Y.; Chen, C. Y.; Su, W. B.; Su, C. H.; Su, A. C. *Acs Nano* **2011**, *5*, 6233.

(21) Clarke, T. M.; Durrant, J. R. *Chem Rev* **2010**, *110*, 6736.

(22) Hains, A. W.; Liang, Z. Q.; Woodhouse, M. A.; Gregg, B. A. *Chem Rev* **2010**, *110*, 6689.

(23) Bredas, J. L.; Norton, J. E.; Cornil, J.; Coropceanu, V. *Accounts Chem Res* **2009**, *42*, 1691.

(24) Haugeneder, A.; Neges, M.; Kallinger, C.; Spirkl, W.; Lemmer, U.; Feldmann, J.; Scherf, U.; Harth, E.; Gugel, A.; Mullen, K. *Phys Rev B* **1999**, *59*, 15346.

(25) Markov, D. E.; Amsterdam, E.; Blom, P. W. M.; Sieval, A. B.; Hummelen, J. C. *J Phys Chem A* **2005**, *109*, 5266.

(26) Theander, M.; Yartsev, A.; Zigmantas, D.; Sundstrom, V.; Mammo, W.; Andersson, M. R.; Inganas, O. *Phys Rev B* **2000**, *61*, 12957.

(27) Keivanidis, P. E. C., T.M.; Lilliu, S.;Agostinelli, T.; Macdonald,J.E.; Durrant,J.R.; Bradley, D.D.C.and Nelson, J. *Physical Chemistry Letters* **2009**, *1*.

(28) Marsh, R. A. H., J.M.; Albert-Seifried, S.;and Friend, R.H. *Nano Letters* **2010**, *10*.

(29) Blakesley, J. C. a. N., D. *Physical Review B* **2011**, *84*.

(30) Giebink, N. C. W., G.P.; Wasielewski, M.R.; and Forrest1, S.R. *Physical Review B* **2010**, *82*.

(31) Dang, M. T.; Hirsch, L.; Wantz, G. *Adv Mater* **2011**, *23*, 3597.

(32) Lee, J. K.; Ma, W. L.; Brabec, C. J.; Yuen, J.; Moon, J. S.; Kim, J. Y.; Lee, K.; Bazan, G. C.; Heeger, A. J. *J Am Chem Soc* **2008**, *130*, 3619.

(33) Moule, A. J.; Meerholz, K. *Adv Mater* **2008**, *20*, 240.

(34) Peet, J.; Kim, J. Y.; Coates, N. E.; Ma, W. L.; Moses, D.; Heeger, A. J.; Bazan, G. C. *Nat Mater* **2007**, *6*, 497.

(35) Zhang, F. L.; Jespersen, K. G.; Bjorstrom, C.; Svensson, M.; Andersson, M. R.; Sundstrom, V.; Magnusson, K.; Moons, E.; Yartsev, A.; Inganas, O. *Adv Funct Mater* **2006**, *16*, 667.

(36) Pingree, L. S. C.; Reid, O. G.; Ginger, D. S. *Nano Lett* **2009**, *9*, 2946.

(37) Campoy-Quiles, M.; Ferenczi, T.; Agostinelli, T.; Etchegoin, P. G.; Kim, Y.; Anthopoulos, T. D.; Stavrinou, P. N.; Bradley, D. D. C.; Nelson, J. *Nat Mater* **2008**, *7*, 158.

(38) Guo, J. M.; Ohkita, H.; Benten, H.; Ito, S. *J Am Chem Soc* **2010**, *132*, 6154.

(39) Chen, D. A.; Nakahara, A.; Wei, D. G.; Nordlund, D.; Russell, T. P. *Nano Lett* **2011**, *11*, 561.

(40) Hallermann, M.; Kriegel, I.; Da Como, E.; Berger, J. M.; von Hauff, E.; Feldmann, J. *Adv Funct Mater* **2009**, *19*, 3662.

(41) Keivanidis, P. E.; Clarke, T. M.; Lilliu, S.; Agostinelli, T.; Macdonald, J. E.; Durrant, J. R.; Bradley, D. D. C.; Nelson, J. *J Phys Chem Lett* **2010**, *1*, 734.

(42) Drummy, L. F.; Davis, R. J.; Moore, D. L.; Durstock, M.; Vaia, R. A.; Hsu, J. W. P. *Chem Mater* **2011**, *23*, 907.

(43) Kozub, D. R.; Vakhshouri, K.; Orme, L. M.; Wang, C.; Hexemer, A.; Gomez, E. D. *Macromolecules* **2011**, *44*, 5722.

(44) Herzing, A. A.; Richter, L. J.; Anderson, I. M. *J Phys Chem C* **2010**, *114*, 17501.

(45) Sundberg, M.; Inganas, O.; Stafstrom, S.; Gustafsson, G.; Sjogren, B. *Solid State Commun* **1989**, *71*, 435.

(46) Cooper, A. I. *J Mater Chem* **2000**, *10*, 207.

(47) Tomasko, D. L.; Li, H. B.; Liu, D. H.; Han, X. M.; Wingert, M. J.; Lee, L. J.; Koelling, K. W. *Ind Eng Chem Res* **2003**, *42*, 6431.

(48) Kikic, I.; Vecchione, F.; Alessi, P.; Cortesi, A.; Eva, F.; Elvassore, N. *Ind Eng Chem Res* **2003**, *42*, 3022.

(49) Alsoy, S.; Duda, J. L. *Chem Eng Technol* **1999**, *22*, 971.

(50) Wells, S. L.; DeSimone, J. *Angew Chem Int Edit* **2001**, *40*, 519.

(51) Walker, T. A.; Frankowski, D. J.; Spontak, R. J. *Adv Mater* **2008**, *20*, 879.

(52) Watkins, J. J.; Brown, G. D.; RamachandraRao, V. S.; Pollard, M. A.; Russell, T. P. *Macromolecules* **1999**, *32*, 7737.

(53) Kirby, C. F.; McHugh, M. A. *Chem Rev* **1999**, *99*, 565.

(54) Asai, S.; Shimada, Y.; Tominaga, Y.; Sumita, M. *Macromolecules* **2005**, *38*, 6544.

(55) Gross, S. M.; Roberts, G. W.; Kiserow, D. J.; DeSimone, J. M. *Macromolecules* **2000**, *33*, 40.

(56) Li, Y.; Wang, X. C.; Sanchez, I. C.; Johnston, K. P.; Green, P. F. *J Phys Chem B* **2007**, *111*, 16.

(57) Ma, W. L.; Yang, C. Y.; Gong, X.; Lee, K.; Heeger, A. J. *Adv Funct Mater* **2005**, *15*, 1617.

(58) Coffey, D. C.; Reid, O. G.; Rodovsky, D. B.; Bartholomew, G. P.; Ginger, D. S. *Nano Lett* **2007**, *7*, 738.

(59) Dante, M.; Peet, J.; Nguyen, T. Q. *J Phys Chem C* **2008**, *112*, 7241.

(60) Muller, C.; Ferenczi, T. A. M.; Campoy-Quiles, M.; Frost, J. M.; Bradley, D. D. C.; Smith, P.; Stingelin-Stutzmann, N.; Nelson, J. *Adv Mater* **2008**, *20*, 3510.

(61) Grancini, G.; Polli, D.; Fazzi, D.; Cabanillas-Gonzalez, J.; Cerullo, G.; Lanzani, G. *J Phys Chem Lett* **2011**, *2*, 1099.

(62) McMahon, D. P.; Cheung, D. L.; Troisi, A. *J Phys Chem Lett* **2011**, *2*, 2737.

(63) Yang, X. N.; Loos, J.; Veenstra, S. C.; Verhees, W. J. H.; Wienk, M. M.; Kroon, J. M.; Michels, M. A. J.; Janssen, R. A. J. *Nano Lett* **2005**, *5*, 579.

(64) Thompson, B. C.; Frechet, J. M. J. *Angew Chem Int Edit* **2008**, *47*, 58.

(65) Kim, J. B.; Allen, K.; Oh, S. J.; Lee, S.; Toney, M. F.; Kim, Y. S.; Kagan, C. R.; Nuckolls, C.; Loo, Y. L. *Chem Mater* **2010**, *22*, 5762.

(66) Palermo, E. F.; Darling, S. B.; McNeil, A. J. *J Mater Chem C* **2014**, *2*, 3401.

(67) Bertho, S.; Janssen, G.; Cleij, T. J.; Conings, B.; Moons, W.; Gadisa, A.; D'Haen, J.; Goovaerts, E.; Lutsen, L.; Manca, J.; Vanderzande, D. *Sol Energ Mat Sol C* **2008**, *92*, 753.

(68) Treat, N. D.; Brady, M. A.; Smith, G.; Toney, M. F.; Kramer, E. J.; Hawker, C. J.; Chabinyc, M. L. *Adv Energy Mater* **2011**, *1*, 145.

(69) Griffini, G.; Douglas, J. D.; Piliego, C.; Holcombe, T. W.; Turri, S.; Frechet, J. M. J.; Mynar, J. L. *Adv Mater* **2011**, *23*, 1660.

(70) Lin, Y.; Lim, J. A.; Wei, Q. S.; Mannsfeld, S. C. B.; Briseno, A. L.; Watkins, J. J. *Chem Mater* **2012**, *24*, 622.

(71) Cheng, Y. J.; Hsieh, C. H.; Li, P. J.; Hsu, C. S. *Adv Funct Mater* **2011**, *21*, 1723.

(72) Gao, D.; Hollinger, J.; Seferos, D. S. *Acs Nano* **2012**, *6*, 7114.

(73) Lee, J. U.; Jung, J. W.; Emrick, T.; Russell, T. P.; Jo, W. H. *J Mater Chem* **2010**, *20*, 3287.

(74) Sivula, K.; Luscombe, C. K.; Thompson, B. C.; Frechet, J. M. J. *J Am Chem Soc* **2006**, *128*, 13988.

(75) Li, A.; Amonoo, J.; Huang, B. Y.; Goldberg, P. K.; McNeil, A. J.; Green, P. F. *Adv Funct Mater* **2014**, *24*, 5594.

(76) He, M.; Han, W.; Ge, J.; Yang, Y. L.; Qiu, F.; Lin, Z. Q. *Energ Environ Sci* **2011**, *4*, 2894.

(77) Gallow, K. C.; Jhon, Y. K.; Genzer, J.; Loo, Y. L. *Polymer* **2012**, *53*, 1131.

(78) Gallow, K. C.; Jhon, Y. K.; Tang, W.; Genzer, J.; Loo, Y. L. *J Polym Sci Pol Phys* **2011**, *49*, 629.

(79) Li, L. S.; Hollinger, J.; Coombs, N.; Petrov, S.; Seferos, D. S. *Angew Chem Int Edit* **2011**, *50*, 8148.

(80) Hollinger, J.; Jahnke, A. A.; Coombs, N.; Seferos, D. S. *J Am Chem Soc* **2010**, *132*, 8546.

(81) Bryan, Z. J.; McNeil, A. J. *Macromolecules* **2013**, *46*, 8395.

(82) Palermo, E. F.; McNeil, A. J. *Macromolecules* **2012**, *45*, 5948.

(83) Locke, J. R.; McNeil, A. J. *Macromolecules* **2010**, *43*, 8709.

(84) Palermo, E. F.; van der Laan, H. L.; McNeil, A. J. *Polym Chem-Uk* **2013**, *4*, 4606.

(85) Okabe, S.; Seno, K.; Kanaoka, S.; Aoshima, S.; Shibayama, M. *Macromolecules* **2006**, *39*, 1592.

(86) Okabe, S.; Seno, K.; Kanaoka, S.; Aoshima, S.; Shibayama, M. *Polymer* **2006**, *47*, 7572.

(87) Merlet-Lacroix, N.; Di Cola, E.; Cloitre, M. *Soft Matter* **2010**, *6*, 984.

(88) Kim, J.; Sandoval, R. W.; Dettmer, C. M.; Nguyen, S. T.; Torkelson, J. M. *Polymer* **2008**, *49*, 2686.

(89) Kim, J.; Zhou, H. Y.; Nguyen, S. T.; Torkelson, J. M. *Polymer* **2006**, *47*, 5799.

(90) Kim, J.; Mok, M. M.; Sandoval, R. W.; Woo, D. J.; Torkelson, J. M. *Macromolecules* **2006**, *39*, 6152.

(91) Hodrokoukes, P.; Floudas, G.; Pispas, S.; Hadjichristidis, N. *Macromolecules* **2001**, *34*, 650.

(92) Xu, Z.; Chen, L. M.; Yang, G. W.; Huang, C. H.; Hou, J. H.; Wu, Y.; Li, G.; Hsu, C. S.; Yang, Y. *Adv Funct Mater* **2009**, *19*, 1227.

(93) Ballantyne, A. M.; Chen, L. C.; Nelson, J.; Bradley, D. D. C.; Astuti, Y.; Maurano, A.; Shuttle, C. G.; Durrant, J. R.; Heeney, M.; Duffy, W.; McCulloch, I. *Adv Mater* **2007**, *19*, 4544.

(94) Heeney, M.; Zhang, W.; Crouch, D. J.; Chabinyc, M. L.; Gordeyev, S.; Hamilton, R.; Higgins, S. J.; McCulloch, I.; Skabara, P. J.; Sparrowe, D.; Tierney, S. *Chem Commun* **2007**, 5061.

(95) Hollinger, J.; DiCarmine, P. M.; Karl, D.; Seferos, D. S. *Macromolecules* **2012**, *45*, 3772.

(96) Tsoi, W. C.; James, D. T.; Domingo, E. B.; Kim, J. S.; Al-Hashimi, M.; Murphy, C. E.; Stingelin, N.; Heeney, M.; Kim, J. S. *Acs Nano* **2012**, *6*, 9646.

(97) Lilliu, S.; Agostinelli, T.; Verploegen, E.; Pires, E.; Hampton, M.; Al-Hashimi, M.; Heeney, M. J.; Toney, M. F.; Nelson, J.; Macdonald, J. E. *Macromol Rapid Comm* **2011**, *32*, 1454.

(98) Hollinger, J.; Gao, D.; Seferos, D. S. *Isr J Chem* **2014**, *54*, 440.

(99) Hollinger, J.; Seferos, D. S. *Macromolecules* **2014**, *47*, 5002.

(100) Ge, J.; He, M.; Xie, N.; Yang, X. B.; Ye, Z.; Qiu, F. *Macromolecules* **2015**, *48*, 279.

(101) Gao, D.; Hollinger, J.; Jahnke, A. A.; Seferos, D. S. *J Mater Chem A* **2014**, *2*, 6058.

(102) Tito, N. B.; Milner, S. T.; Lipson, J. E. G. *Macromolecules* **2010**, *43*, 10612.

(103) Lefebvre, M. D.; de la Cruz, M. O.; Shull, K. R. *Macromolecules* **2004**, *37*, 1118.

(104) Cowan, S. R.; Roy, A.; Heeger, A. J. *Phys Rev B* **2010**, *82*.

(105) Maurano, A.; Hamilton, R.; Shuttle, C. G.; Ballantyne, A. M.; Nelson, J.; O'Regan, B.; Zhang, W. M.; McCulloch, I.; Azimi, H.; Morana, M.; Brabec, C. J.; Durrant, J. R. *Adv Mater* **2010**, *22*, 4987.

(106) Maurano, A.; Shuttle, C. C.; Hamilton, R.; Ballantyne, A. M.; Nelson, J.; Zhang, W. M.; Heeney, M.; Durrant, J. R. *J Phys Chem C* **2011**, *115*, 5947.

(107) Shuttle, C. G.; O'Regan, B.; Ballantyne, A. M.; Nelson, J.; Bradley, D. D. C.; Durrant, J. R. *Phys Rev B* **2008**, *78*.

(108) Sweetnam, S.; Graham, K. R.; Ndjawa, G. O. N.; Heumuller, T.; Bartelt, J. A.; Burke, T. M.; Li, W. T.; You, W.; Amassian, A.; McGehee, M. D. *J Am Chem Soc* **2014**, *136*, 14078.

(109) Lange, I.; Kniepert, J.; Pingel, P.; Dumsch, I.; Allard, S.; Janietz, S.; Scherf, U.; Neher, D. *J Phys Chem Lett* **2013**, *4*, 3865.

(110) Lilliu, S.; Agostinelli, T.; Pires, E.; Hampton, M.; Nelson, J.; Macdonald, J. E. *Macromolecules* **2011**, *44*, 2725.

(111) Segalman, R. A.; McCulloch, B.; Kirmayer, S.; Urban, J. J. *Macromolecules* **2009**, *42*, 9205.

(112) McCullough, R. D. *Adv Mater* **1998**, *10*, 93.

(113) Nonnenmacher, M.; Oboyle, M. P.; Wickramasinghe, H. K. *Appl Phys Lett* **1991**, *58*, 2921.

(114) Melitz, W.; Shen, J.; Kummel, A. C.; Lee, S. *Surf Sci Rep* **2011**, *66*, 1.

(115)Hoppe, H.; Glatzel, T.; Niggemann, M.; Hinsch, A.; Lux-Steiner, M. C.; Sariciftci, N. S. *Nano Lett* **2005**, *5*, 269.

(116)Clack, N. G.; Salaita, K.; Groves, J. T. *Nat Biotechnol* **2008**, *26*, 825.

(117)Moores, B.; Hane, F.; Eng, L.; Leonenko, Z. *Ultramicroscopy* **2010**, *110*, 708.

(118)Hane, F.; Moores, B.; Amrein, M.; Leonenko, Z. *Ultramicroscopy* **2009**, *109*, 968.

(119)Cabral, J. T.; Gerard, H.; Clarke, N.; Higgins, J. S. *Physica B* **2000**, *276*, 408.

(120)Pham, J. Q.; Green, P. F. *Macromolecules* **2003**, *36*, 1665.

(121)Kim, E.; Krausch, G.; Kramer, E. J.; Osby, J. O. *Macromolecules* **1994**, *27*, 5927.

(122)Sugimura, H.; Hayashi, K.; Saito, N.; Nakagiri, N.; Takai, O. *Appl Surf Sci* **2002**, *188*, 403.

(123)Liscio, A.; Palermo, V.; Fenwick, O.; Braun, S.; Mullen, K.; Fahlman, M.; Cacialli, F.; Samori, P. *Small* **2011**, *7*, 634.

(124)Kelvin, L. *Philosophical Magazine Series 5* **1898**, *46*, 82.

(125)Sadewasser, S.; Glatzel, T.; SpringerLink (Online service); Springer-Verlag Berlin Heidelberg: Berlin, Heidelberg, 2012.

(126)Glatzel, T.; Sadewasser, S.; Lux-Steiner, M. C. *Appl Surf Sci* **2003**, *210*, 84.

(127)Shen, Y.; Barnett, D. M.; Pinsky, P. M. *The Review of scientific instruments* **2008**, *79*, 023711.

(128)Neff, J. L.; Rahe, P. *Phys Rev B* **2015**, *91*.

(129)Barth, C.; Foster, A. S.; Henry, C. R.; Shluger, A. L. *Adv Mater* **2011**, *23*, 477.

(130)Barth, C.; Henry, C. R. *Phys Rev Lett* **2007**, *98*.

(131)Binnig, G.; Quate, C. F.; Gerber, C. *Phys Rev Lett* **1986**, *56*, 930.

(132)Giessibl, F. J.; Bielefeldt, H.; Hembacher, S.; Mannhart, J. *Appl Surf Sci* **1999**, *140*, 352.

(133)Garcia, R.; Perez, R. *Surf Sci Rep* **2002**, *47*, 197.

(134) Kelley, T. W.; Granstrom, E. L.; Frisbie, C. D. *Adv Mater* **1999**, *11*, 261.
(135) Mativetsky, J. A.; Palma, M.; Samori, P. *Top Curr Chem* **2008**, *285*, 157.